

Chaos and secular evolution of triaxial N -body galactic models due to an imposed central mass

C. Kalapotharakos^{1,2}, N. Voglis¹, and G. Contopoulos¹

¹ Academy of Athens, Research Center for Astronomy, 4 Soranou Efessiou Str., Athens, 11527, Greece
e-mail: [ckalapot;nvoglg;gcontop]@cc.uoa.gr

² University of Athens, Department of Physics, Section of Astrophysics, Greece

Accepted 18 June 2004 / Accepted 20 August 2004

Abstract. We investigate the response of triaxial non-rotating N -body models of elliptical galaxies with smooth centers, initially in equilibrium, under the presence of a central mass assumed to be due mainly to a massive central black hole. We examine the fraction of mass in chaotic motion and the resulting secular evolution of the models. Four cases of the size of the central mass are investigated, namely $m = 0.0005, 0.0010, 0.0050, 0.0100$ in units of the total mass of the galaxy. We find that a central mass with value $m < 0.005$ increases the mass fraction in chaotic motion from the level of 25–35% (that appears in the case of smooth centers) to the level of 50–80% depending on the value of m and on the initial maximum ellipticity of the system. However, most of this mass moves in chaotic orbits with Lyapunov numbers too small to develop chaotic diffusion in a Hubble time. Thus their secular evolution is so slow that it can be neglected in a Hubble time.

Larger central masses ($m \geq 0.005$) give initially about the same fractions of mass in chaotic motion as for smaller m , but the Lyapunov numbers are concentrated to larger values, so that a secular evolution of the self-consistent models is prominent. These systems evolve in time tending to a new equilibrium. During their evolution they become self-organized by converting chaotic orbits to ordered orbits of the Short Axis Tube type. The mechanism of such a self-organization is investigated. The rate of this evolution depends on m and on the value of the initial maximum ellipticity of the system. For $m = 0.01$ and a large initial maximum ellipticity $E_{\max} \approx 7$, equilibrium can be achieved in one Hubble time, forming an oblate spheroidal configuration. For the same value of m and initial maximum ellipticity $E_{\max} \approx 3.5$, or for $E_{\max} \approx 7$, but $m = 0.005$, oblate equilibrium configurations can also be achieved, but in much longer times. Furthermore, we find that, for $m = 0.005$ and $E_{\max} \approx 3.5$, triaxial equilibrium configurations can be formed. The fraction of mass in chaotic motion in the equilibrium configurations is in the range of 12–25%.

Key words. chaos – stellar dynamics – methods: N -body simulations – galaxies: formation – galaxies: evolution – galaxies: kinematics and dynamics

1. Introduction

From the decade of 60 s it has been known that at the centers of galaxies black holes possibly exist. The presence of black holes was proposed, at first, to explain the Active Galactic Nuclei (AGNs) (Salpeter 1964; Zeldovich 1964; Lynden-Bell 1969). But during the last decade, due to higher quality observations (HST), many researchers (Kormendy & Richstone 1995; Kormendy et al. 1997; Faber et al. 1997; van der Marel et al. 1997, 1998; Kormendy et al. 1998; Magorrian et al. 1998; Cretton & van den Bosch 1999; Verdoes Kleijn et al. 1999; Gebhardt et al. 2000b) found, evidence for the existence of large black holes at the centers of galaxies. Nowadays, the dominant opinion is that almost all galaxies contain a super-massive black hole at their centers.

N -body simulations of cosmological disipationless collapses give systems that resemble non-rotating elliptical

galaxies with smooth centers, i.e. the potential well near the center is approximately of harmonic oscillator type. The system forms a triaxial configuration of particles. Let the Cartesian coordinates x, y, z be oriented along the shortest axis (a), the intermediate axis (b) and the longest axis (c), respectively. The majority of the ordered orbits of stars in such a system can be classified in four types. Namely, **Box** orbits, **Inner Long Axis Tube** orbits (ILAT), **Outer Long Axis Tube** orbits (OLAT) and **Short Axis Tube** orbits (SAT) (de Zeeuw 1985; Statler 1987).

The Box orbits fill a box resembling a parallelepiped with curved sides. The larger and the smaller dimension of the box are respectively along the longest and the shortest axis of the system. A Box orbit can pass arbitrarily close to the center of the galaxy.

The ILAT orbits fill a space elongated along the longest axis of the system having a hole along the same axis. In many cases the hole is small and the corresponding ILAT orbits resemble

to the Box orbits. For this reason we call them also box-like orbits (Contopoulos et al. 2002). Such orbits can also approach the center at small distances.

The SAT orbits are close to circular orbits surrounding the shortest axis x of the system. They fill a tube-like region not very extensive along the shortest axis. They support an oblate spheroidal configuration, or they reduce the elongation of the triaxial figure created by the box and box-like orbits. Their frequencies of oscillation along the y and z axes have an 1:1 ratio. For this reason they are frequently called 1:1 resonant tube orbits in order to be distinguished from higher order resonant tube orbits.

As regards the chaotic motions the above systems develop a modest level of chaos. In Voglis et al. 2002, (hereafter VKS) we found that in these systems a fraction of mass of about 25–35% of their total mass moves in chaotic orbits with Lyapunov Characteristic Numbers (LCN) rarely exceeding the value of 10^{-1} (in units of the inverse radial period corresponding to a value of energy equal to the potential at the half mass radius). We found also that only a fraction less than 8% belongs to orbits that can develop chaotic diffusion in a Hubble time ($LCN > 10^{-2}$). The chaotic orbits, in general, change their geometry in time between geometries close to box and SAT orbits, tending to fill the whole space inside the equipotential surfaces which are more round than the equidensity surfaces.

The presence of a central mass, (a central black hole or a central density cusp) produces a significant number of chaotic orbits in galaxies with triaxial shape (see, for example, Gerhard & Binney 1985; Merritt & Fridman 1996; Merritt & Valluri 1996; Fridman & Merritt 1997; Valluri & Merritt 1998; Siopis & Kandrup 2000; Poon & Merritt 2001; Kandrup & Sideris 2002; Kandrup & Siopis 2003). The reason is that the box and the box-like orbits, which are mainly responsible for the triaxiality, are scattered by the central mass and become chaotic tending to fill the space inside the equipotential surface defined by their energy. Therefore, they have rounder shapes than that of their host galaxy. Thus, if a triaxial galaxy consists mainly of chaotic orbits, it cannot be self-consistent, unless it is not in an equilibrium state. In fact a triaxial galaxy with many chaotic orbits is not in equilibrium in general, but it evolves towards an equilibrium configuration. As we will see later, such an equilibrium, under certain conditions, can be triaxial, but in principle, it is close to an axisymmetric oblate spheroidal configuration. In any case the equilibrium structure of the system is mainly supported by ordered orbits of a tube type, with large enough angular momentum, so that the orbits avoid approaching the center.

On the other hand attempts to construct self-consistent triaxial galaxies with central mass, using the Schwarzschild's method (Schwarzschild 1979; Merritt & Fridman 1996; Siopis 1999), indicated that ordered orbits alone could not produce self-consistent solutions for such models. For this reason people included also chaotic orbits. Nevertheless, the models constructed were not “fully” stationary, especially in the case of a strong cusp.

The dynamical effects of a central mass on a galaxy depends on the relative mass parameter, i.e. the ratio $m = M_{\text{cm}}/M_{\text{g}}$, of the value of the Central Mass M_{cm} to the total

mass of the galaxy M_{g} . M_{cm} stands for the sum of all the types of mass that can contribute to a central concentration, e.g. a supermassive black hole, dense star clusters, large molecular concentrations, etc. However, our main interest is concentrated on the case where a black hole is the main component of the central mass. Thus, we choose central mass models with a concentrated rather than a dispersed character.

In VKS we used N -body simulations to construct self-consistent models of non-rotating triaxial elliptical galaxies with smooth centers. Two models were used, produced from cosmological initial conditions, consistent with a power law spectrum $P(k) \propto k^n$ of the density perturbation field with $n = -2$. One of them, called Q (produced from quiet initial conditions) is characterized by the presence of a strong non-rotating bar and a high ratio of radial to tangential velocity dispersion. The other one, called C (produced from clumpy initial conditions), is more spherical and has a lower ratio of radial to tangential velocity dispersion.

In the present paper we extend our investigation in the case of self-consistent non-rotating models of triaxial elliptical galaxies with central mass.

For this purpose and in order to make a direct comparison with the cases of smooth centers, we have used the same N -body models (Q and C, used in VKS) to create a number of models by inserting a central mass with various values of the relative mass parameter m . Our main interest is concentrated on the evolutionary features of the systems and the mechanism by which a self-consistent evolution proceeds.

Namely, the questions we try to investigate are: Under a given value of m

- (i) For how long galaxies can maintain a triaxial shape?
- (ii) What is the structure of phase space at various stages of the evolution and how is it transmuted towards a final configuration?
- (iii) What fraction of mass moves in chaotic orbits at a given snapshot and how this fraction of mass evolves in time?
- (iv) By which mechanism initially triaxial galaxies can relax to equilibrium configurations under the presence of a massive central mass?

In Sect. 2 a more detailed description of the models used is given. In Sect. 3 the evolutionary features of the models in terms of their ellipticities and triaxiality index are described. In Sect. 3.1 a number of numerical tests are given showing that the results obtained are stable under different values of the run parameters. Phase space structures at particular snapshots are examined in Sect. 4. In Sect. 5 the methods used to detect ordered and chaotic orbits are outlined and the results regarding the fraction of mass in chaotic motion in every model are discussed. The models with larger values of m tend to be self-organized. The mechanism of this process is discussed in Sect. 6. Finally, our main conclusions are presented and discussed in Sect. 7.

2. Description of the models

Before the description of our models we make some useful comments regarding the scaling units used and the time scales

of the problem. The unit of length is the half mass radius R_h of the smooth center models Q and C. The unit of energy is defined so that the deepest value of the potential in these models is $V_0 = -100$. The unit of time is the half mass crossing time, defined by

$$T_{\text{hmct}} = \left(\frac{2R_h^3}{GM_g} \right)^{\frac{1}{2}}. \quad (1)$$

The circular period T_{cp} , at a radius R_h , is

$$T_{\text{cp}} = 2\pi T_{\text{hmct}}. \quad (2)$$

The relation between the radial period T_r of an orbit (the time needed for a star to go from the pericentre to the apocentre and back to the pericentre of its orbit) and the circular period T_{cp} of the same energy can be written as

$$T_{\text{cp}} = fT_r \quad (3)$$

where the factor f is $f = 1$ in the Keplerian potential, and $f = 2$ in the harmonic potential. In the potential of our N -body systems f ranges between these two values. For orbits of the N -body systems with energies near the value of the potential at the half mass radius, the values of f are close to 2. For these orbits also the radial period T_r is

$$T_r \approx 3T_{\text{hmct}}. \quad (4)$$

A star in circular motion, in a typical galaxy, describes about 50 cycles in a Hubble time t_{Hub} . Therefore, a Hubble time can be written as

$$t_{\text{Hub}} \approx 50T_{\text{cp}} = 50fT_r \approx 300T_{\text{hmct}}. \quad (5)$$

At a run time of $100T_{\text{hmct}}$ the smooth center models Q and C, considered in VKS, are in a well established virial equilibrium. There are only some very small time variations of their potential.

Starting from the final snapshot of this run time, by setting $t = 0$, two families of new models are derived by adding an extra central potential to their gravitational field, that is supposed to be due to a Central Mass (CM). For this purpose, we have adopted the model potential proposed by Allen et al. (1990). Namely,

$$V_{\text{cm}}(r) = \frac{GM_{\text{cm}}}{a} \left[\arctan\left(\frac{r}{a}\right) - \frac{\pi}{2} \right] \quad (6)$$

where a is a softening length given by

$$a = 0.05 \frac{M_{\text{cm}}}{M_g} R_g = 0.05mR_g \quad (7)$$

where R_g is the radius of the galaxy.

The density corresponding to this potential is given by the formula

$$\rho_{\text{cm}}(r) = \frac{GM_{\text{cm}}a^2}{2\pi r(r^2 + a^2)^2}, \quad (8)$$

and corresponds to a cuspy profile r^{-1} very near to the center.

The corresponding force is

$$F_{\text{cm}}(r) = -\frac{GM_{\text{cm}}}{r^2 + a^2}, \quad (9)$$

i.e. it is of a Keplerian nature only for orbits with pericentres much larger than a . The force at the center of this model tends to a finite constant. Stars with pericentres below the softening length a are not deflected strongly by the central mass. The effect of different values of a is discussed in Sect. 3.1.

We examine four cases regarding the relative mass parameter m , i.e. the ratio $m = M_{\text{cm}}/M_g$. Namely, we examine models with values $m = M_{\text{cm}}/M_g = (0.0005, 0.001, 0.005, 0.01)$ resulting from both the Q and the C systems. Thus, including the original models with the smooth centers ($m = 0$), we have a series of ten models to compare. We call these models Q000, Q005, Q010, Q050, Q100, and C000, C005, C010, C050, C100, respectively. (The letter declares the source model (Q or C) and the subsequent number declares the value of m in units of $1/10000$).

Our systems are composed of $\sim 1.5 \times 10^5$ particles. We run them by the conservative technique code of Allen et al. (1990), hereafter APP-code. This code evolves every system in a self-consistent way. The corresponding potential is expressed as an expansion in a bi-orthogonal basis of spherical Bessel functions and spherical harmonics. The coefficients are re-evaluated at time steps of $\Delta t = 0.025T_{\text{hmct}}$. For the needs of our problem here, where forces can be quite large when orbits pass close to the center, we have improved the integration scheme of the original version of the code by using a symplectic 4th order integrator with readjustable time step.

In real galaxies, the value of the central mass may be a function of time. Here, we only examine cases in which the time of growth of a central mass is much less than a Hubble time, so that the establishment of the central mass can be considered abrupt.

3. Effects due to a central mass

In our triaxial systems (principal axes: shortest, middle, longest, a , b , c , along the coordinates x , y , z), we define the ellipticities

$$E_{xz} = 10(1 - a/c), \quad E_{yz} = 10(1 - b/c), \quad E_{xy} = 10(1 - a/b) \quad (10)$$

corresponding to the projections of the equidensity surfaces on the principal planes. These ellipticities are evaluated by a method similar to the method proposed by Athanassoula et al. (1990). Namely, in order to evaluate, for example, E_{yz} of the equidensity surface with axes a , b , c , we consider that the projection of this surface on the plane yz (principal plane) is given by the formula

$$\left(\frac{y - y_0}{b} \right)^s + \left(\frac{z - z_0}{c} \right)^s = 1. \quad (11)$$

(Notice that the projections on the principal planes do not alter the size of the axes.) For a particular equidensity contour, the simplex method is used to define the values of the parameters b , c , y_0 , z_0 , s for which a best fit of this contour is obtained.

We examine the dependence of the ellipticities on the length of the projected major axis r of the equidensity surface on each plane, at a time $t = 150$ after the central mass is inserted.

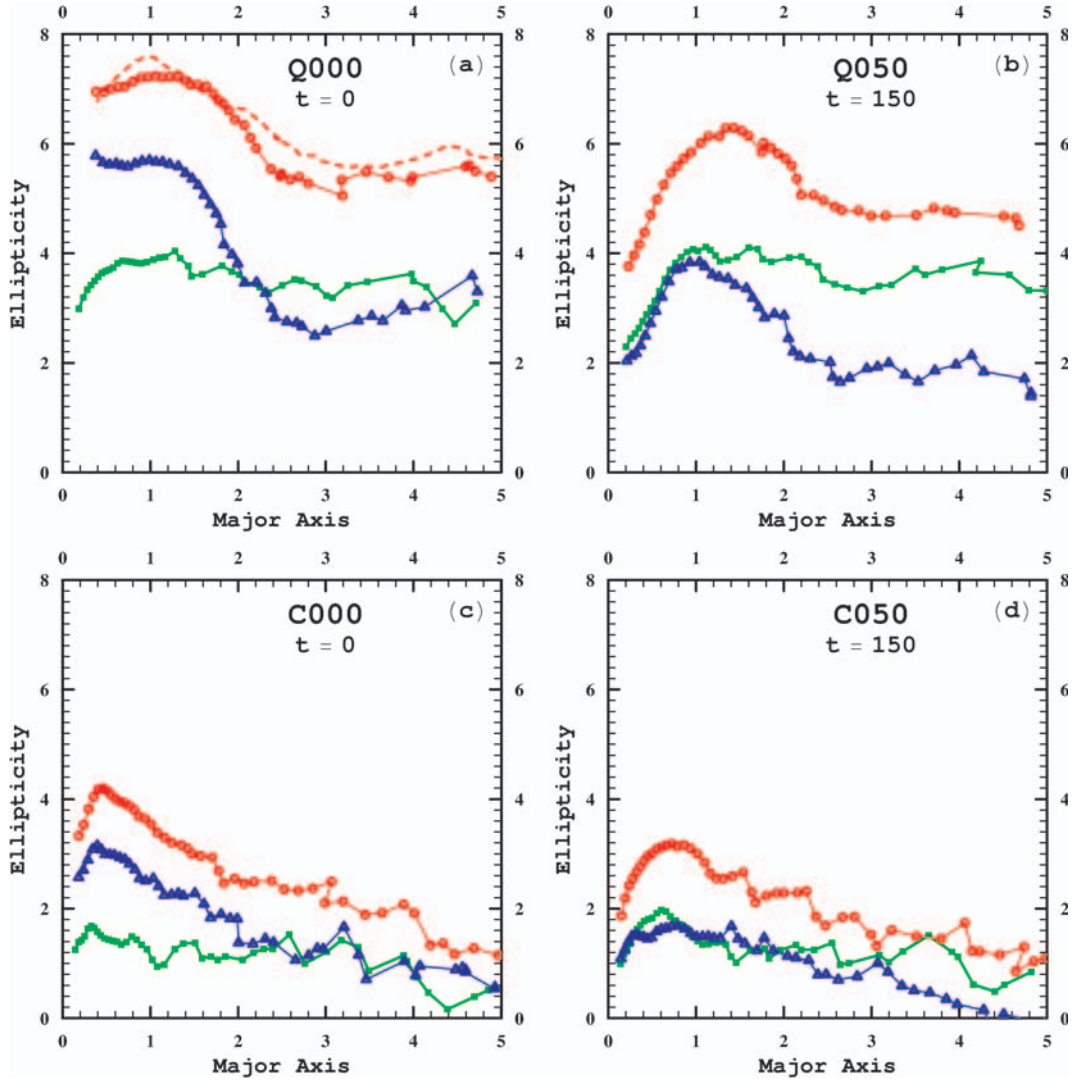


Fig. 1. a), b), c), d) The ellipticities E_{xz} (red circles), E_{yz} (blue triangles), E_{xy} (green squares) as functions of the projected major axis, for the models Q000, Q050, C000, C050 at the time $t = 0$ and $t = 150$ as indicated in the figures. The ellipticities E_{xz} and E_{yz} are more sensitive than E_{xy} under the presence of a central mass with $m = 0.005$. The dashed line close to the curve of E_{xz} in a) gives the same function of E_{xz} as it is derived from the data of the tree code after the collapse and relaxation of the system from cosmological initial conditions as described in VKS. This line is drawn as a test of the results of the APP-code and it is discussed in Sect. 3.1.

In Figs. 1a–d we see, for comparison, the ellipticities along the major axis of the models Q000, Q050 and C000, C050, respectively. Open circles correspond to the projection on the xz plane (red line), triangles to the yz plane (blue line), and bold squares to the xy plane (green line). In the smooth center models (Figs. 1a,c, Q000, C000) the ellipticities are larger in the inner parts (at $r \approx 1$), with a maximum ellipticity on the xz plane (open circles) of about 7 for Q000 and of about 4 for C000. In the outer parts ($r \approx 3.5$) the maximum ellipticities are by 1 or 2 units smaller. Under the presence of a central mass (of relative mass $m = 0.005$ (Figs. 1b,d, Q050, C050) the ellipticities on the xz and yz planes become smaller. In the inner parts ($r \approx 1$), the maximum ellipticity is reduced by about 1 unit. In the outer parts the effect is smaller. Under the presence of the central mass, the ellipticity on the yz plane (middle-long axes) appears more sensitive. The ellipticity on the xy plane (short-middle axes) is not sensitive, remaining almost the same in

Q000 and Q050, as well as in C000 and C050 (compare the green lines with bold squares in Figs. 1a and b, as well as in Figs. 1c and d).

In Figs. 2a,b we give the three ellipticities as functions of the relative value m of the central mass for those equidensity surfaces which have major axis of length $r = 1$ and $r = 3.5$, respectively, in the Q family of models, at $t = 150$. In all cases of m the ellipticities E_{xz} (red circles) and E_{yz} (blue triangles) decrease with increasing m , with E_{yz} being more sensitive. The ellipticity E_{xy} (green squares) remains almost constant. This behavior of the ellipticities means that the presence of a central mass mainly affects the axial ratio on the middle-longest axes plane. In other words the bar-like character of the configuration projected on this plane is reduced.

Similar remarks can be made in the case of the C family models (Figs. 2c,d).

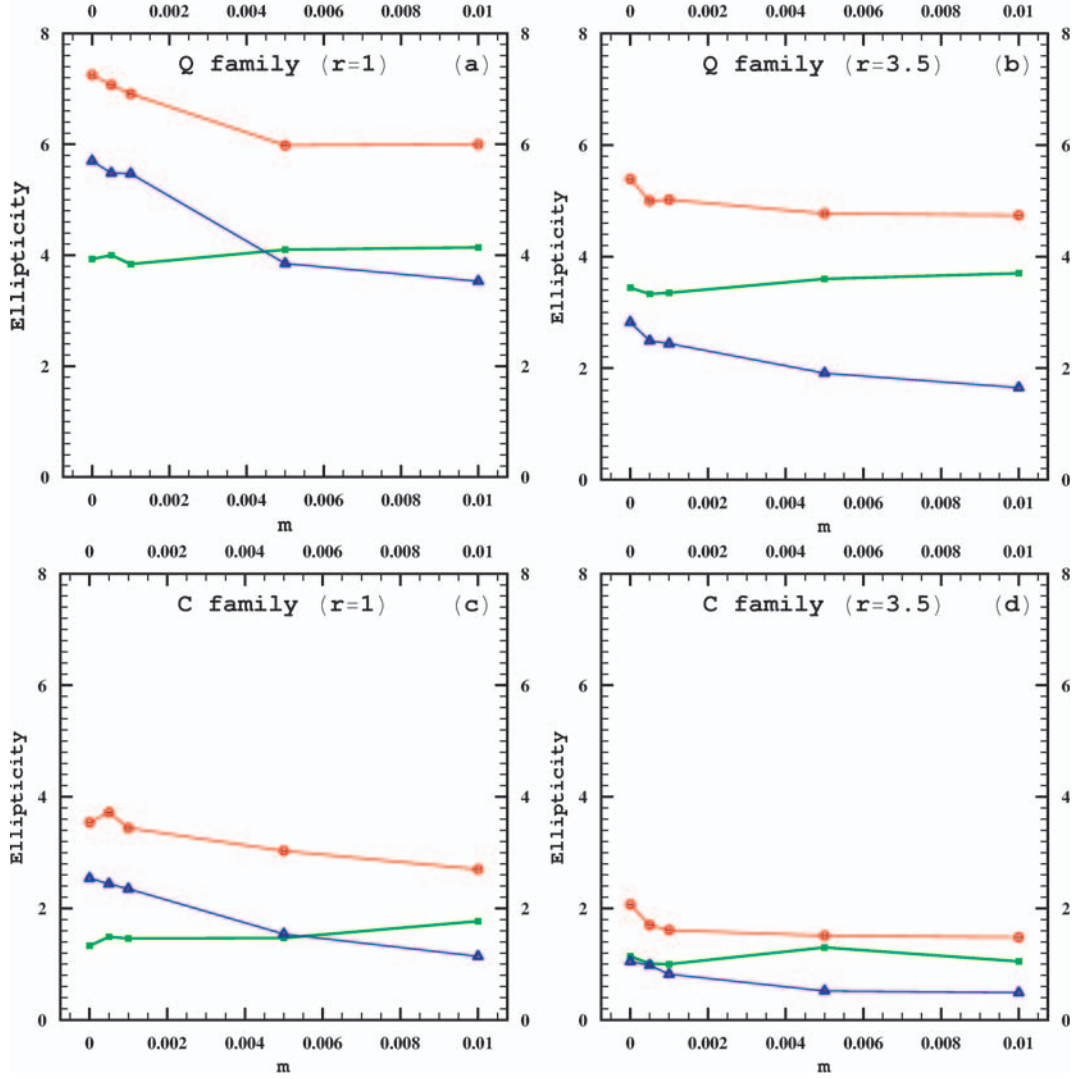


Fig. 2. a), b), c), d) The ellipticities E_{xz} (red circles), E_{yz} (blue triangles), E_{xy} (green squares) at two values of the projected major axis $r = 1$ and $r = 3.5$ as functions of m in all the Q family and C family models, as indicated in the figure, at $t = 150$. The ellipticity E_{xy} is almost independent of m , while the other ellipticities decrease with m .

It is interesting to examine the time evolution of the triaxiality and of the maximum ellipticity of our systems for various values of m . The triaxiality is measured by the index T

$$T = \frac{c^2 - b^2}{c^2 - a^2} = \frac{1 - (1 - E_{yz}/10)^2}{1 - (1 - E_{xz}/10)^2} = \frac{(E_{yz} - 20)E_{yz}}{(E_{xz} - 20)E_{xz}}. \quad (12)$$

In an oblate axisymmetric configuration the index T is equal to 0, while it is equal to 1 in a prolate axisymmetric configuration. In a maximally triaxial configuration it takes the value of 0.5. The main features of the shape of an equidensity surface are determined by the value of T and the value of its maximum ellipticity E_{\max} . Each triaxial ellipsoid is represented by one point on the $E_{\max} - T$ diagram.

The smooth center models Q000 and C000, in the inner parts, are triaxial configurations but with a prolate character. Namely, for the equidensity surfaces with longest axis equal to $r = 1$, the triaxiality index is $T \simeq 0.9$ in Q000 and $T \simeq 0.8$ in C000. In their outer parts, they are close to maximally triaxial configuration. The shape of these models is almost

permanent in time. In the corresponding models with a central mass both the maximum ellipticity E_{\max} and the triaxiality index T decrease in time.

In what follows the maximum ellipticity E_{\max} and the triaxiality index T are evaluated from the equidensity surfaces with their longest axis equal to $r = 1$.

In Fig. 3 the evolution on the plane $E_{\max} - T$ is shown for the models Q010, Q050, Q100 (black solid lines) and the models C050, C100 (dashed red lines). The evolution of a system follows a line in Fig. 3 downwards. In the Q family models E_{\max} starts from a value of $\simeq 7$, while in the C family E_{\max} starts from $\simeq 3.5$. In Q050 and Q100 models the maximum ellipticities approach a final value of about 4, while in the C050 and C100 they reach a final value of about 2. A big blue dot on each curve in Fig. 3 corresponds to the values reached in a Hubble time by the respective models. Only the Q100 model has achieved the final value of $E_{\max} \simeq 4$ in a Hubble time, while in the Q050 model E_{\max} is still above a value of 5 and in the Q010 it is very close to the initial value.

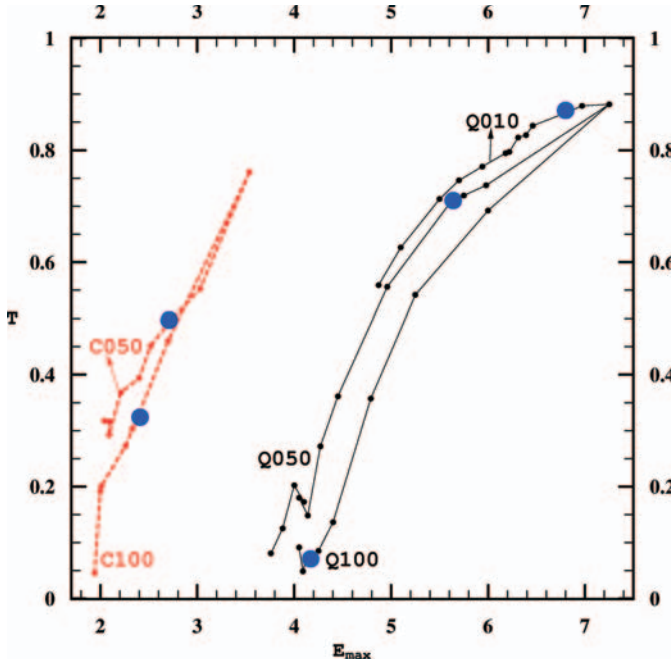


Fig. 3. Lines of evolution on the plane of maximum ellipticity – triaxiality index ($E_{\max} - T$) corresponding to the indicated models Q010, Q050, Q100 (black solid lines) and the models C050, C100 (dashed red lines). A big blue dot on each curve shows the point reached by the respective model in one Hubble time. The evolution is downwards.

Notice that the values of the final maximum ellipticities (4 in the Q family and 2 in the C family) are almost equal to the ellipticity E_{xy} which, as we have seen above (green line in Figs. 2a–d), is almost independent of the value of the central mass. This ellipticity is also almost independent of time, since it maintains a value close to the corresponding ellipticity of the smooth center case. It seems that the equilibrium configuration is obtained when the maximum ellipticity of a system with central mass meets the value of E_{xy} of the smooth center case.

The triaxiality index T as a function of time is plotted in Fig. 4 for the same models. For large values of the relative mass m , the time evolution of T becomes a sensitive function of m .

In the smooth center case Q000, evolved for about 6 Hubble times ($t \approx 1800$, in Fig. 4), the triaxiality index remains constant near the value of about 0.9. In the Q010 case, T , starting from this value, decreases very slowly. It falls to a value of about 0.55 after 20 Hubble times ($t \approx 6000$, in Fig. 4). Its decrease in a Hubble time is negligible. Similar is the behavior of T in the corresponding models of the C family (C000, C010, not drawn in Fig. 4).

In the cases of Q050 and Q100, however, T follows an almost linear decrease down to a small value (close to zero), at which value it remains roughly constant. These systems have reached a shape close to an oblate spheroidal equilibrium configuration. For the Q050 model this occurs in about 6 Hubble times, while for the Q100 model it is much faster occurring only in about one Hubble time.

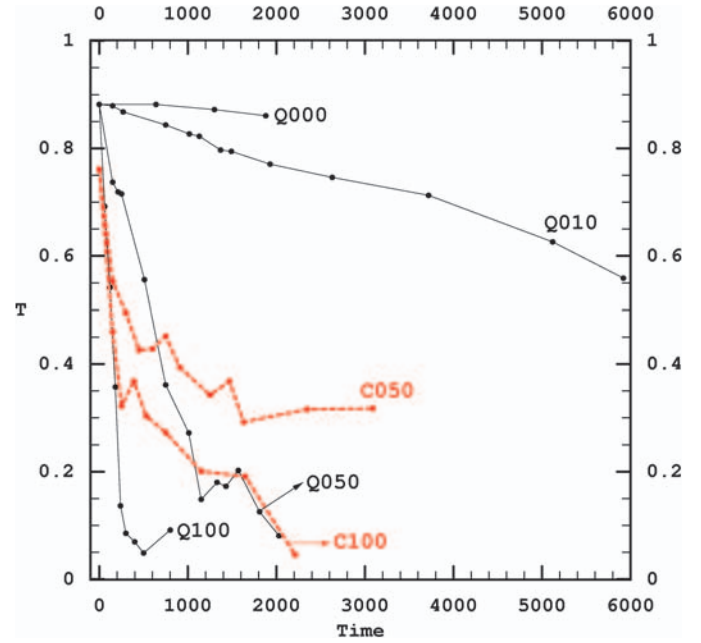


Fig. 4. Time evolution of the triaxiality index T of the models Q000, Q010, Q050, Q100 (black solid lines) and the models C050, C100 (dashed red lines). The secular evolution is fast for $m \geq 0.005$ leading the corresponding models to an equilibrium with constant T . An oblate spheroidal equilibrium can be obtained in a Hubble time only in Q100. In Q050, C100 it can be obtained but in longer times. In C050 the triaxiality index remains well above zero indicating that a central mass in this case is compatible with triaxial shapes.

In the C050 and C100 models two different rates of decrease of T appear. An initial fast evolution (lasting for about one Hubble time) in which T decreases from the initial value of about 0.8 to a value of about 0.5 (in C050), or 0.4 (in C100). In the subsequent evolution the rate of decrease of T slows down. In the C100 model the triaxiality continues decreasing until an equilibrium configuration with almost zero value of T is obtained after about 7 Hubble times. In the C050 model the values of T continue decreasing but they do not go to zero. They are saturated at a value of about 0.3, reflecting the fact that a triaxial equilibrium configuration is obtained. This requires about 6 Hubble times. This result indicates that there must be a threshold value on m , below which the presence of a central mass can be compatible with triaxial equilibrium configuration. Such a threshold is expected to be different in systems resembling the Q model than in systems resembling the C model. In other words, the maximum value of m , allowing triaxial figures of equilibrium, must depend on the particular initial ratio of the radial to the tangential kinetic energy of the system.

The compatibility of the presence of a massive central mass with a modest or a maximal triaxiality of the system is also supported by the results of Poon & Merritt (2002, 2004), who find that stable triaxial configuration in system with cuspy density profiles can exist.

Regarding the evolution of our systems in one Hubble time we conclude from the description above that a central mass of relative mass $m = 0.01$ is marginally capable to change,

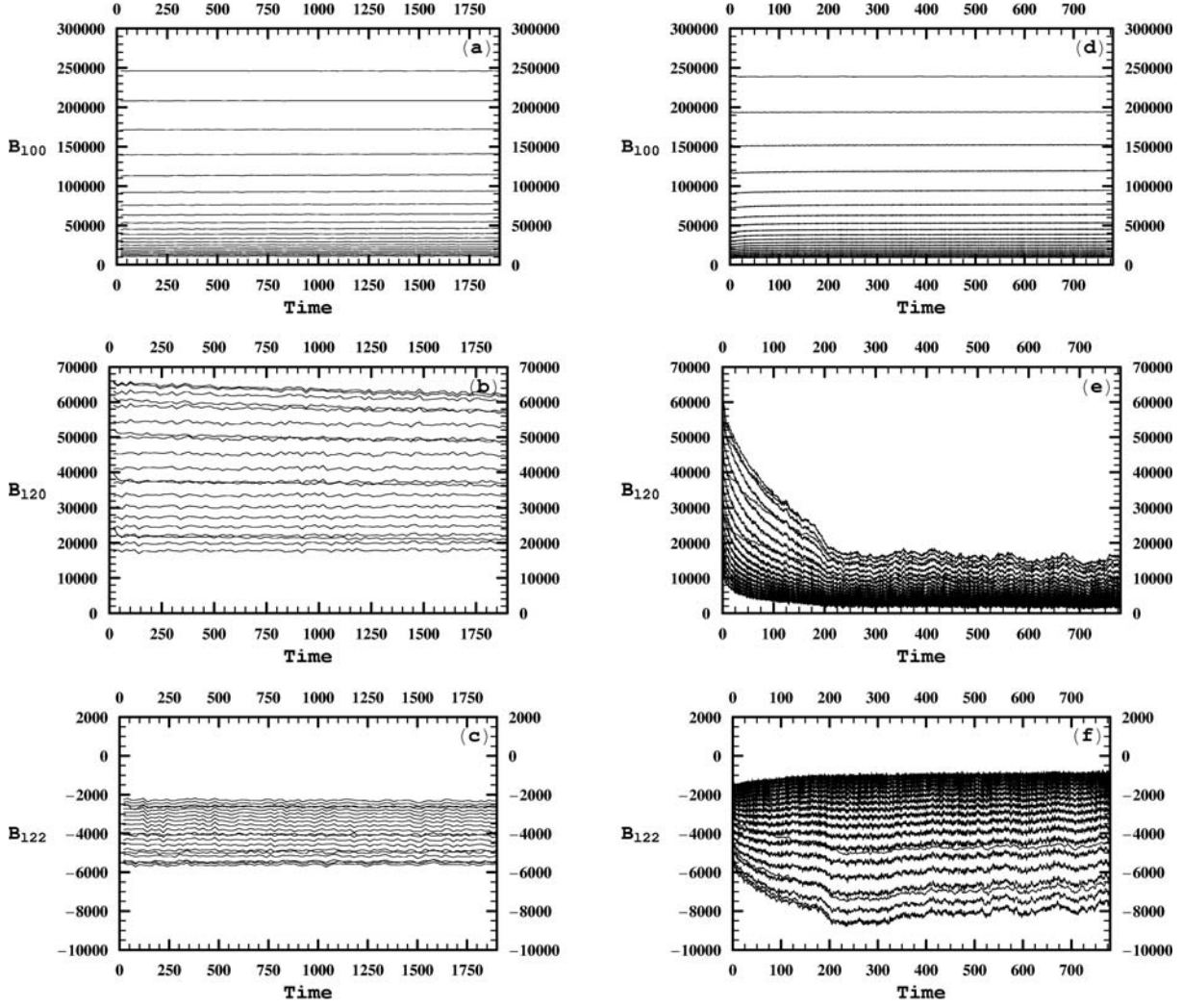


Fig. 5. a)–c) Time evolution of the most important coefficients of the expansion of the self-consistent potential in the Q000 model. These coefficients remain remarkably constant. d)–f) The evolution of the coefficients of the same type as in a)–c) but for the Q100 model. The quadrupole coefficients B_{120} and the coefficients of the triaxial terms B_{122} evolve considerably in time in the Q100 model, reflecting the secular evolution of the shape of this model.

in one Hubble time, a non-rotating elliptical galaxy to an oblate spheroidal equilibrium configuration.

For smaller relative masses (e.g. $m \cong 0.005$), galaxies can have a secular evolution towards an equilibrium configuration that is not necessarily of the oblate spheroidal type, but it can maintain a good level of triaxiality.

For even smaller values of m (e.g. $m \leq 0.001$) the changes on the triaxiality in a Hubble time are negligible.

The above results are in agreement with the results given by Merritt & Quinlan (1998), according to which the shape of a galaxy with $m \leq 0.003$ evolves in time scales that exceed 100 orbital periods.

The secular evolution of the models with central mass can also be considered in terms of the coefficients in the expansion of the self-consistent potential of the N -body system provided by the APP-code. This potential given in terms of spherical Bessel functions and spherical harmonics contains

20 monopole terms, 20 quadrupole terms and 80 triaxial terms. In spherical coordinates (r, θ, ϕ) it can be written as

$$\begin{aligned}
 V(r, \theta, \phi) = & \underbrace{\sum_{l=0}^{19} B_{l00} V_{l00}(r)}_{20 \text{ monopole terms}} + \underbrace{\sum_{l=0}^{19} B_{l20} V_{l20}(r, \theta)}_{20 \text{ quadrupole terms}} \\
 & + \sum_{l=0}^{19} B_{l21} V_{l21}(r, \theta) \cos \phi + \sum_{l=0}^{19} C_{l21} V_{l21}(r, \theta) \sin \phi \\
 & + \underbrace{\sum_{l=0}^{19} B_{l22} V_{l22}(r, \theta) \cos 2\phi + \sum_{l=0}^{19} C_{l22} V_{l22}(r, \theta) \sin 2\phi}_{80 \text{ triaxial terms}} \quad (13)
 \end{aligned}$$

where $B_{l00}, B_{l20}, B_{l21}, C_{l21}, B_{l22}, C_{l22}$, with $l = 0, \dots, 19$ are the corresponding coefficients. In a self-consistent run these coefficients are re-evaluated at regular small time steps.

In Figs. 5a–f the coefficients of the most important terms ($B_{l00}, B_{l20}, B_{l22}$, with $l = 0, \dots, 19$) are plotted as functions of

time for a period of about 6 Hubble times in the model Q000 (left column) and of about 3 Hubble times in the model Q100 (right column). In the case of Q000 (Figs. 5a–c) all the coefficients are remarkably constant throughout this long evolution (for this reason we only plot their values every $20 T_{\text{hmct}}$).

In the case of Q100 (Figs. 5d–f) the coefficients are plotted at every time step ($0.025 T_{\text{hmct}}$). The monopole terms B_{l00} (Fig. 5d) in this case also remain remarkably constant in time. The coefficients of the quadrupole terms (B_{l20} , Fig. 5e), however, show a serious decrease in their size (reduced to about 1/3 of their initial values) in a period of about a Hubble time. After that, they remain roughly constant (with variations around their mean values less than 10%, which, however, are of the order of less than 1% with respect to the total value of the potential). Since the quadrupole coefficients measure actually the strength of the bar, it is clear that the bar becomes considerably more weak at the end of a Hubble time. A central mass of relative mass $m = 0.01$, or more, can destroy the bar-like configuration of an elliptical galaxy in a Hubble time.

As regards the coefficients of the triaxial terms, the most important of them are the coefficients B_{l22} shown in Figs. 5c,f. All the other coefficients are considerably smaller. Comparing the coefficients B_{l22} of the Q000 model (Fig. 5c) with B_{l22} in the Q100 model (Fig. 5f) we see that the coefficients with larger absolute values show an increase of their absolute values by about 50%. This corresponds to the fact that the potential deepens along the y -axis and becomes more shallow along the x -axis.

So far we have shown that the shape of the system Q100, driven by the central mass, changes (slowly) from a prolate configuration (high triaxiality index) with maximum ellipticity E7 to an oblate configuration (almost zero triaxiality index) with maximum ellipticity E4. This evolution is also expressed by the time variations of the coefficients in the expansion of the self-consistent potential. In Sect. 6 we discuss the mechanism by which this transformation occurs.

3.1. Testing the numerical results

A number of tests are discussed in this section in order to check the accuracy and the stability of our results. The tests refer (1) to the reliability of the APP-code, (2) to the process of integration of the orbits in a time varying potential and the effect of the integration time step, (3) to the effect of the softening length a of the central mass and (4) to the effect of the number of radial terms of the code and the effect of a larger number of particles.

(1) Testing the reliability of the APP-code.

Two strong indications show that the code can be reliable for the problem faced here. First is the fact all the coefficients of the expansion in the potential remain constant in Q000 for periods much longer than a Hubble time (Figs. 5a–c). No systematic error is accumulated, otherwise the system could not be in such a stable equilibrium.

Second, the APP-code agrees with the tree code in the cases that we have checked. E.g. we found that the APP-code preserves the shape of the systems resulting from the tree-code that is used in VKS to create the equilibrium configurations from cosmological initial conditions (see Sect. 1). As an

example, from the initial equilibrium configuration created by the tree code we derived the ellipticity E_{xz} as a function of the major axis in the case of the Q000 model and we plotted this curve in Fig. 1a as a dashed line. This line has only small differences in comparison with the curve of the same quantity E_{xz} (red circles) corresponding to the snapshot of the output of the APP-code after a long run of $100 T_{\text{hmct}}$.

(2) Testing the accuracy of integration in a time varying potential.

To test this accuracy we do the following: the coefficients of the potential are updated every $\Delta t = 0.025 T_{\text{hmct}}$. The integration of the orbits during this small period is done with constant coefficients and with locally readjustable time steps to ensure that the relative variation of the energy of the orbit is $\frac{\Delta E}{E} \leq 2.5 \times 10^{-7}$ in the interval Δt . At the end of each Δt the coefficients of the potential are re-evaluated. On the other hand the relative change of the energy $\frac{\Delta E}{E}$ due to the slowly varying potential is in the range of 10^{-4} to 10^{-1} . This is much larger than the tolerance of the energy in the process of integration of the orbits.

We have checked also that an integration time step Δt five times smaller gives almost identical results.

(3) Testing the effect of different values of the softening length a .

In order to check the effect of the softening length a of the central mass, we have performed another two runs for the Q100 model with different values of a . Namely, a run with $a = 0.005 m R_g$, i.e. 10 times smaller and a run with $a = 0.5 m R_g$, i.e. 10 times larger than the value $a = 0.05 m R_g$ proposed by Allen et al. (1990).

In the case of $a = 0.005 m R_g$ we have almost identical results with those for $a = 0.05 m R_g$. In the case of $a = 0.5 m R_g$, that corresponds to a rather dispersed central mass, the system tends to relax to about the same final configuration but in much longer time. The effect of the central mass is now considerably slower. The delay is due to the fact that the Lyapunov numbers are smaller and the chaotic diffusion is slower.

From these tests we conclude that the adopted value of $a = 0.05 m R_g$ is a good choice to describe the efficiency of a not very dispersed central mass that is produced mainly by a central black hole. The results presented in the paper are quite stable as regards the size of the softening length in this region of values.

(4) Testing the effect of the number of terms in the potential and of the number of particles.

From these tests we can state that by increasing the number of particles our results do not change appreciably except of the decrease of the level of noise. On the other hand, increasing the number of radial functions in the potential causes an acceleration on the rate at which the system Q100 tends to the final equilibrium configuration. If we increase the number of radial terms from $l = 20$ terms to $l = 50$ terms, this acceleration reduces the time required to reach equilibrium by 15%. On the contrary a decrease of the number of terms from $l = 20$ to $l = 10$ increases the time for equilibrium by a factor of 2. This comparison shows that the time scale for the establishment of the equilibrium tends to saturate as the number of radial terms increases. At any rate the time found for $l = 20$ is of the correct order of magnitude. It is important to stress the fact that the

resulting final equilibrium configuration is always almost exactly the same.

4. Phase space structure at particular snapshots

If we are interested in studying a particular snapshot of the evolution of our systems, we fix the values of the coefficients in the expansion of the potential at a given time and write an autonomous 3D Hamiltonian. This Hamiltonian in cylindrical coordinates (R, ϕ, z) can be written as

$$H = \frac{\dot{R}^2}{2} + \frac{L_z^2}{2R^2} + \frac{\dot{z}^2}{2} + V(R, z) + V_1(R, \phi, z) + V_{\text{cm}}(r) \quad (14)$$

where $r = \sqrt{R^2 + z^2}$. The term $V(R, z)$ is the axisymmetric part of the potential (13), containing the monopole and the quadrupole terms only, and $V_1(R, \phi, z)$ is the triaxial part of this potential. L_z is the component of the angular momentum of a particle along the z axis.

If we neglect the triaxial term of the potential $V_1(R, \phi, z)$ we can write a 2D autonomous Hamiltonian on a meridian plane

$$H = \frac{\dot{R}^2}{2} + \frac{L_z^2}{2R^2} + \frac{\dot{z}^2}{2} + V(R, z) + V_{\text{cm}}(r) \quad (15)$$

in which L_z is an integral of motion.

The above Hamiltonians are useful in studying the phase space structure of our systems at a given snapshot. A similar technique has been used by Contopoulos et al. (2002) in order to examine the phase space structure of such systems and the foliation of the invariant tori of the orbits described by their particles due to the third integral.

Consider a set of test particles with energy $H = -35$ and initial conditions $(x, y, z, \dot{x}, \dot{y}, \dot{z}) = (0, y, 0, 0, 0, \dot{z}(H))$ uniformly distributed along the y -axis and their velocities along the z -axis (zero angular momentum along z , i.e. $L_z = 0$). These test particles in the Hamiltonian (15) move on the yz -plane.

In Fig. 6a we plot the Poincaré surface of section (y, \dot{y}) for $z = 0$ and $\dot{z} > 0$ of these orbits in the Hamiltonian (15) applied to the potential of the Q000 model at a snapshot at $t = 0$. (Because of the symmetry we only plot the Poincaré consequents for $y > 0$ and we use R and $V_R = \dot{R}$ instead of (y, \dot{y}) . The velocity unit in Fig. 6 is equal to the rms velocity of the particles in Q000). In Fig. 6a the invariant curves surrounding the origin $(0, 0)$ and having R less than about 0.5 correspond to box orbits. On the other hand, the invariant curves surrounding the point $(R \simeq 1.0, V_R = 0.0)$ form an island corresponding to the 1:1 resonant orbits. In between these two types of invariant curves there is a chaotic layer and a number of islands corresponding to higher resonant orbits.

We run the above set of test particles (the same initial conditions) in the 3D Hamiltonian (14) applied to the triaxial form of the potential of the Q000 model at the same snapshot as above. The Poincaré surface of section in this case is 4-dimensional (x, y, \dot{x}, \dot{y}) with $z = 0$ and $\dot{z}(H) > 0$. The corresponding Poincaré consequents, projected on the (R, V_R) plane, are plotted in Fig. 6b. Although the orbits are not any more confined on the yz plane the projections of their consequents on the two dimensional surface (R, V_R) maintain a very good

level of foliation of the corresponding invariant tori. Diffusion due to the higher dimensionality is very small. The tori of box orbits appear for R less than about 0.5. The other set of tori that form an island of ordered motion around $R \approx 1.0$ correspond to the 1:1 resonant orbits that do not spread arbitrarily far from the yz plane and they are characterized as Short Axis Tube (SAT) orbits. These SAT orbits are separated from the box orbits by a chaotic layer.

Figures 6c,d are similar to Figs. 6a,b, but they refer to the case of the Q010 model ($m = 0.001$) at the snapshot $t = 150$ after inserting the central mass. It is clear in these figures that the invariant tori of the box orbits have been destroyed by the presence of the central mass. The area of the box orbits in Figs. 6a,b has become a chaotic area in Figs. 6c,d. This chaotic area is united with the chaotic layer surrounding the island of the 1:1 resonant orbits in Figs. 6a,b. It is remarkable that inside the chaotic area produced by the previously ordered box orbits, some tori forming islands of resonant orbits survive. This occurs because such resonant orbits avoid passing very close to the center, thus they are not scattered by the central mass.

For the same reason the invariant tori of the SAT orbits survive. Moreover, their stability is further increased by the central mass, as we can infer from the enlargement of their island of ordered motion by comparing Fig. 6b with Fig. 6d. Notice that for larger m the SAT orbits start appearing at lower energy levels than for smaller m .

We have constructed several diagrams similar to Figs. 6a–d for various energy levels and values of L_z for models of various m at their snapshot $t = 150$. From these diagrams it becomes clear that, as m increases, the area of ordered motion in SAT orbits increases, while the area of chaotic motion (coming from the destruction of the tori of box or box-like orbits) decreases. As an example, we give in Figs. 7a,b the results obtained from the Hamiltonian (15) applied to the models C100 and C010 with the initial conditions of the test particles described above and for $H = -90$. The area of SAT orbits in the C100 model (Fig. 7a) is much larger than the corresponding area in the C010 model (Fig. 7b). The organization of motion in SAT orbits proceeds much faster in the former case than in the latter case. The chaotic area in C100 is much smaller than in C010. Since the two models have the same origin it is clear that a production of order out of chaos has occurred, which is very prominent in the case of C100. Then, as a consequence of the second thermodynamical law, the remaining chaotic orbits acquire larger Lyapunov Numbers, as we will see in the next sections.

5. Mass component in chaotic motion

5.1. The method of detecting the mass in chaotic motion

In VKS we have introduced a method to distinguish between the mass in chaotic motion and the mass in ordered motion in N -body systems like those described here. This method combines different tools. One tool is what we call Finite Time Specific Lyapunov Characteristic Number (FT-SLCN), or simply L_j . This quantity is the mean rate of divergence of

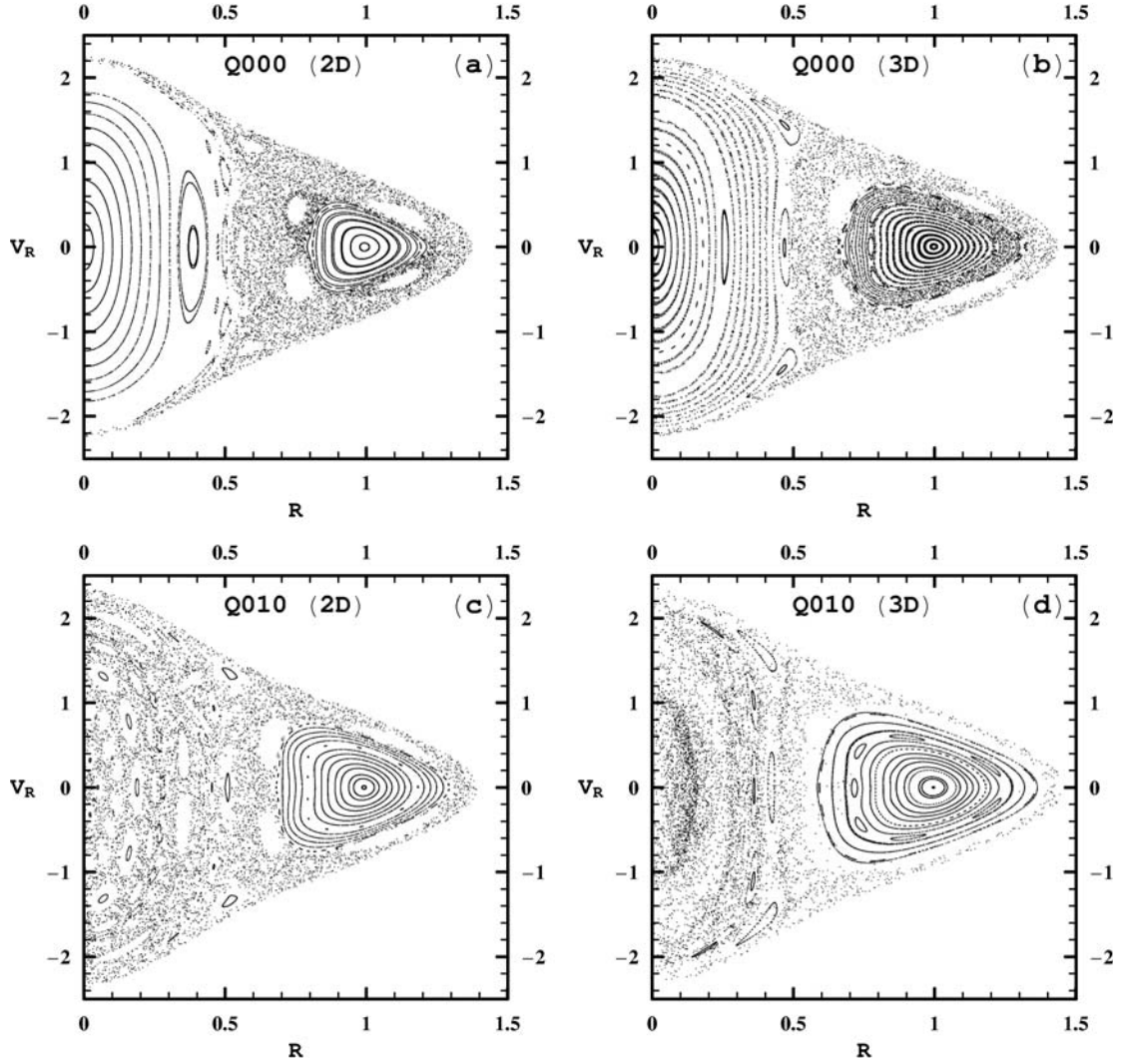


Fig. 6. **a)** Poincaré surface of section (PSOS) on $z = 0$ with $\dot{z} > 0$ for a set of test particles with energy $H = -35$ and initial conditions $(x, y, z, \dot{x}, \dot{y}, \dot{z}) = (0, y, 0, 0, 0, \dot{z}(H))$ uniformly distributed along the y axis, in the Hamiltonian (15) applied to the Q000 model at $t = 0$. Because of the symmetry of the potential we only plot the consequents for $y > 0$ and we use the symbols $(R, V_R = \dot{R})$ instead of (y, \dot{y}) . The area of Box orbits corresponds to the invariant curves for $R \leq 0.5$ and the area of the 1:1 tube orbits corresponds to the invariant curves around the periodic orbit at $(R \approx 1.0, V_R = 0.0)$. Chaotic orbits form a layer between these two types of regular orbits. **b)** The projection on the (R, V_R) plane of the 4-dimensional PSOS derived from the 3D Hamiltonian (14) applied to the Q000 model with the same energy and initial conditions of test particles as in **a)**. This figure has many similarities with **a)** because diffusion due to higher dimensionality is small. The 1:1 tube orbits in **a)** are now replaced by the SAT orbits. **c)** As in **a)** but for the model Q010 at $t = 150$. The area of Box orbits is converted to an area of chaotic orbits because of the presence of a central mass with $m = 0.001$. This chaotic area is united with the chaotic layer surrounding the island of the 1:1 tube orbits. This island appears larger than in **a)**. An number of resonant Box orbits survive as indicated by the small islands in the region of $R \leq 0.5$. **d)** As in **b)** but for the model Q010 at $t = 150$. The island of SAT orbits survives and increases in size while all the area of Box orbits in **b)** is now chaotic except of some areas of higher resonant orbits.

neighboring orbits, in units of the inverse radial period of every orbit, calculated for a fixed number N_{rp} of radial periods. (If N_{rp} tends to infinity, L_j tends to the maximal Lyapunov Characteristic Number, LCN.)

In the case of ordered motion, L_j takes values that are almost independent of the characteristic time scales of the particular orbit and decreases in average as N_{rp}^{-1} .

Whenever the value of L_j along an orbit takes a roughly constant value, not decreasing any more with time, we infer that the orbit is chaotic, with a specific LCN approximately equal

to this constant value. If L_j continues to decrease as N_{rp}^{-1} until the maximum number of radial periods is achieved the orbit is considered (conventionally) as an ordered orbit. In fact, along ordered orbits L_j tends to zero as N_{rp} tends to infinity.

If the LCN of a chaotic orbit is of the order of 10^{-n} , then this LCN is detectable only if N_{rp} is larger than 10^n . By fixing N_{rp} , the minimum value of a detectable LCN is also fixed. In our applications below we use $N_{\text{rp}} = 1200$ and only LCNs larger than $10^{-2.8}$ (in units of the inverse radial periods) are detectable. The behavior of chaotic orbits having LCNs smaller

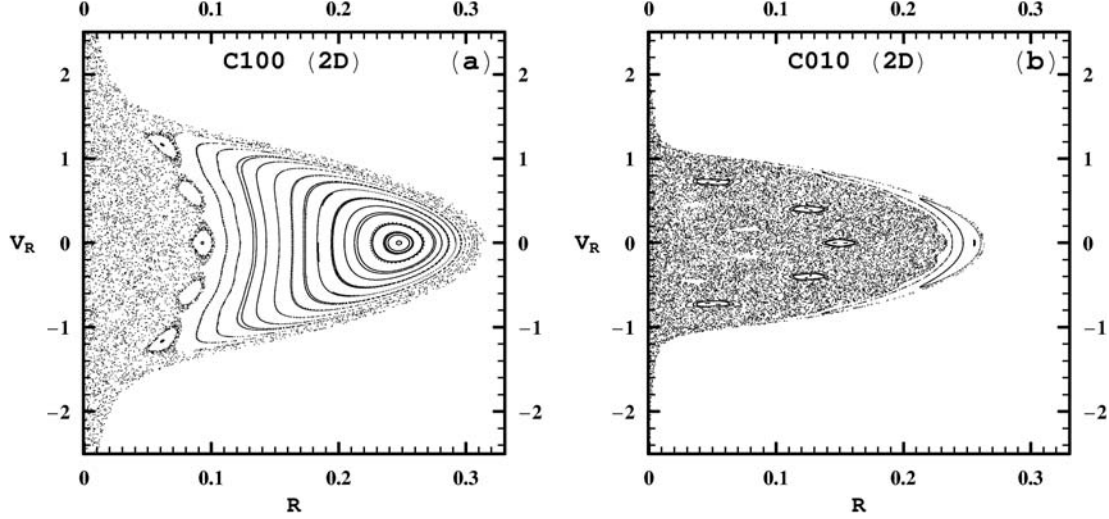


Fig. 7. a), b) As in Fig. 6c but for the models C100 and C010, respectively, at the energy level of $H = -90$. The organization of motion in SAT orbits proceeds much faster in the model C100 a) than in the model C010 b).

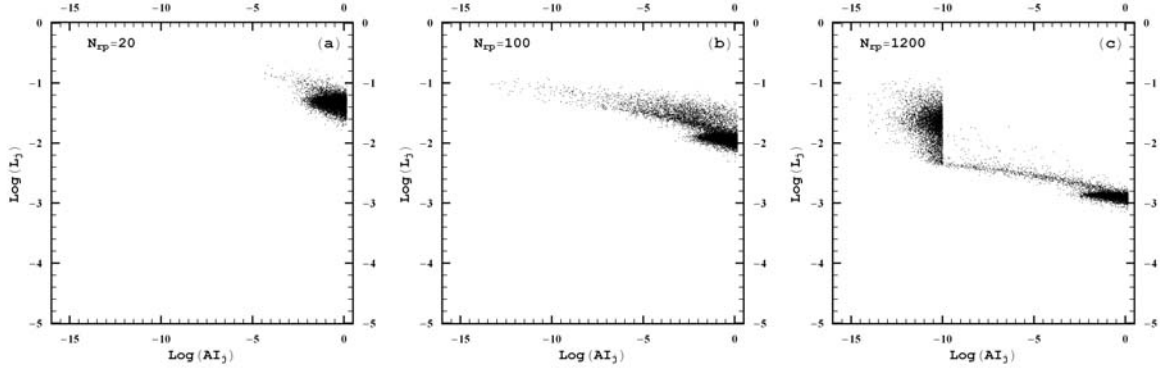


Fig. 8. Separation of the chaotic from the ordered orbits on the plane of $\log(AI_j) - \log(L_j)$. a) For $N_{\text{tp}} = 20$ no separation can be obtained. Almost all the orbits are grouped in a triangular area with large AI_j . b) For $N_{\text{tp}} = 100$ the orbits with $\log(L_j) > -1.8$ are separated from the triangular area tending to form a group of chaotic orbits. c) For $N_{\text{tp}} = 1200$ the orbits with $\log(L_j) > -2.8$ are separated. They form a group of chaotic orbits with $AI_j < 10^{-10}$ and a lane of weakly chaotic orbits joining this group with the triangular area of ordered orbits or orbits with smaller values of $\log(L_j)$. The sharp edge on the right side of the chaotic group in explained in the text.

than this limit is in practice so close to ordered orbits for times of about 10^3 radial periods, that, in a good approximation, they can be considered as ordered orbits.

Using L_j we can only decide whether an orbit should be classified as ordered or chaotic within the detection limit. The values of L_j do not express directly the efficiency of chaotic diffusion in a Hubble time because they are not expressed in common units. For this reason we use also the Finite Time LCN in common units, or simply $L_{\text{cu}j}$. As a common unit, the inverse radial period of an orbit with energy equal to the mean value of the potential at the half mass radius is used.

In parallel to the above tools, another tool is used called the alignment index (AI_j). It has been shown (Voglis et al. 1998, 1999; Skokos 2001) that in a 3D autonomous Hamiltonian system, two arbitrary deviation vectors $\xi_{j1}(t)$ and $\xi_{j2}(t)$ of the same orbit j , as they evolve along the orbit, behave in a different way with respect to each other if the orbit is ordered than if the orbit is chaotic. Namely, if the orbit is chaotic, the two deviation vectors tend exponentially to acquire the same

direction (parallel or antiparallel), pointing along the direction of the invariant manifold with the largest real eigenvalue. If the two deviation vectors are normalized to unity, the amplitude of their difference (if they are parallel), or of their sum (if they are antiparallel) called Alignment Index (AI_j), i.e.

$$AI_j = |\xi_{j1}(t) \mp \xi_{j2}(t)| \quad (16)$$

tends exponentially to zero.

On the other hand, if the orbit is ordered the two deviation vectors oscillate around each other. In this case AI_j varies around a finite mean value that remains always not very far from unity (it almost never becomes less than 10^{-3}).

In Figs. 8a–c we give on the $\log(AI_j) - \log(L_j)$ plane an example of separation of the chaotic from the ordered orbits in the Q100 model resulting from the Hamiltonian (14), when it is applied at a snapshot of its secular evolution at $t = 150$ (after inserting the central mass).

For a number of radial periods $N_{\text{tp}} = 20$, (Fig. 8a) almost all the orbits of the particles of the system are concentrated

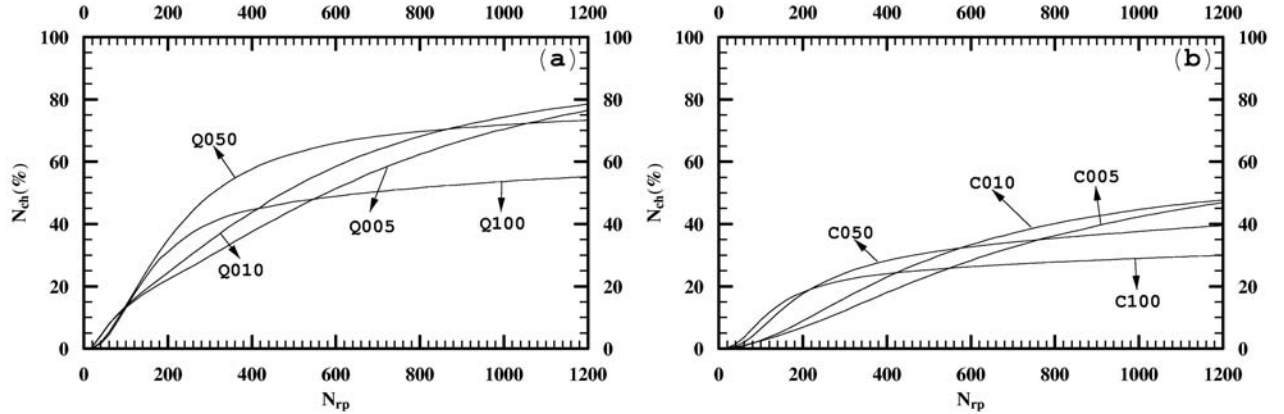


Fig. 9. a), b) The increase of the detected mass fraction in chaotic motion as a function of the number of radial periods N_{rp} for the snapshot at $t = 150$ of various models of the Q family a) and of the C family b) as indicated in the figures.

in a triangular region with $\log(L_j)$ between -1 and -2 and $\log(AI_j) > -3$. No distinction between ordered and chaotic orbits can be made for this value of N_{rp} . For $N_{rp} = 100$, the particles in chaotic motion with $\log(L_j) > -1.8$ have been separated from the triangular region (Fig. 8b), while for $N_{rp} = 1200$ the particles in chaotic motion separated from the triangular region have $\log(L_j) > -2.8$ (Fig. 8c). The orbits that remain in the triangular region in Fig. 8c correspond either to particles in ordered motion or to particles in chaotic motion with $\log(L_j) < -2.8$. Of course, this limit can be pushed down to lower values just by increasing the number of radial periods N_{rp} . However, further changes of the distribution of particles become quite slow. For this reason we consider here this limit as adequate and all the orbits with $\log(L_j) < -2.8$ as ordered orbits.

Most of the chaotic orbits in Fig. 8c have very small values of AI_j (smaller than 10^{-10}), forming a group of chaotic orbits with values above $L_j \approx 10^{-2.4}$ and a mean value of L_j about $10^{-1.6}$. Notice that, for a number of these chaotic orbits the values of AI_j become smaller than 10^{-10} before the number of radial periods $N_{rp} = 1200$ is achieved. Thus, one can decide about the character of these orbits at smaller values of N_{rp} and there is no need for the integration to go on. It is stopped just when $AI_j \leq 10^{-10}$. This is why the right hand side of the group of chaotic orbits in Fig. 8c is sharp.

In Fig. 8c there is also a lane of points joining the above group with the group of ordered motion in the triangular region with $AI_j > 10^{-3}$ and $L_j \approx 10^{-3}$. This lane corresponds to more weakly chaotic orbits, or to sticky chaotic orbits that are trapped temporarily between invariant tori or cantori before they enter a chaotic sea.

Using the above method we can build a library of particles in the whole system that are located at chaotic orbits in the frozen potential of a particular snapshot. Another library for the same system can be created by repeating this process in the frozen potential of another snapshot. Then, we can compare the two libraries both as regards the total number and the identities of particles in chaotic motion.

Such a comparison was made in VKS between two different snapshots of the Q000 model differing by a time interval of $\Delta t = 100T_{\text{hmct}}$. It was found that the identities of less than 3%

of the particles were different in the two libraries, due mainly to the level of noise in the coefficients of the potential rather than to some evolutionary process. As we will see below the models with the largest m give libraries of particles in chaotic motion with considerably larger differences due to secular evolution of these models.

5.2. The detected fractions of mass in chaotic motion at given snapshots

We first apply this method in all of our models to separate the mass in chaotic motion from the mass in ordered motion with their potential fixed at the snapshot of $t = 150$.

In Figs. 9a,b we see how the fraction of the detected mass in chaotic motion increases by increasing the N_{rp} . The tendency of this fraction to saturate with increasing N_{rp} is clear in these diagrams. (Notice that the increase of the fraction of mass in chaotic motion with N_{rp} is only due to the increase of the threshold that separates the two types of motion and has nothing to do with the secular evolution of the systems in time. What we find here is only the fraction of mass in chaotic motion that is compatible with the adopted frozen potential).

For $N_{rp} = 1200$ the detected mass in chaotic motion is on the level of 70–80% of the total mass in the models Q005, Q010, Q050, while it is on the level of 55% in the Q100 model (Fig. 9a).

We conclude that the mass component in chaotic motion, that is compatible with their potential at isochronous snapshots, is not a monotonic function of the value of the central mass. A similar behavior appears in the C family of models. In C005, C010, C050 the mass components in chaotic motion is on the level of 40–50%, while in C100 it is on the level of 30% (Fig. 9b).

In Fig. 10a we give the proportion of chaotic orbits as a function of m , including the smooth center cases Q000 and C000 ($m = 0$). In this figure the solid line corresponds to the Q family and the dashed line to the C family. In the Q family the mass component in chaotic motion, (in a potential corresponding to isochronal evolution of the systems, $t = 150$), starts from a value of about 35% in the smooth center case, increases with increasing m to a maximum value of about 80% at $m = 0.001$ and then decreases to 55% for $m = 0.01$. Similar is

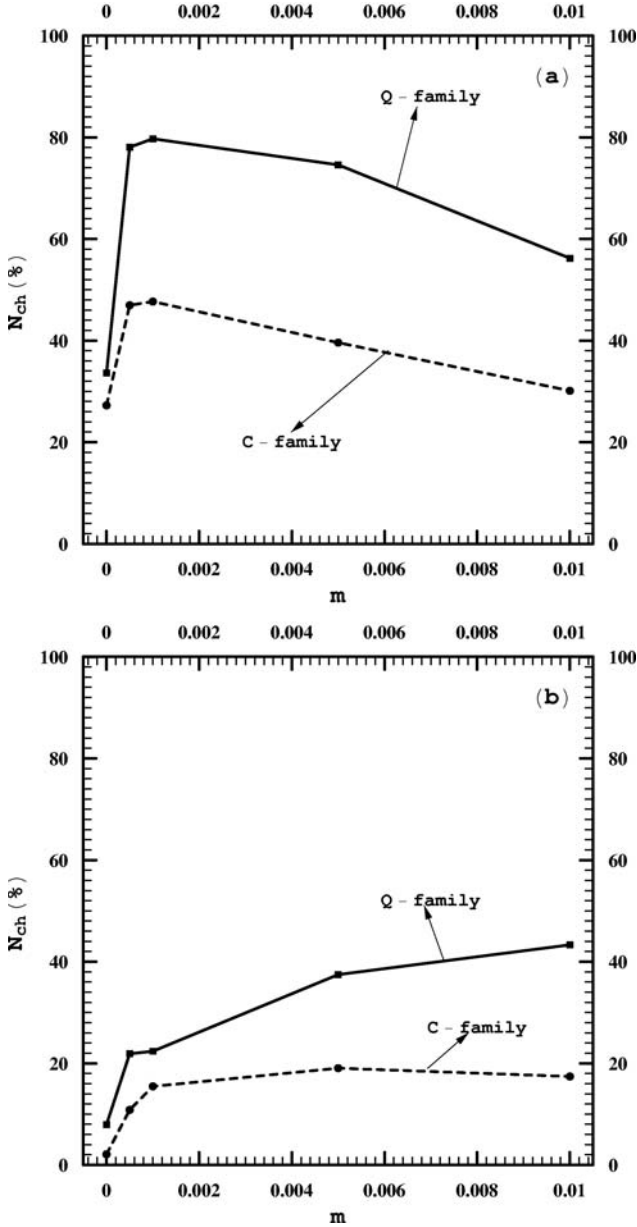


Fig. 10. **a)** The fraction of mass in chaotic motion at $t = 150$ as a function of the relative mass m of the central mass. For $m > 0.001$ the chaotic mass decreases with m because of the self-organization. **b)** The fraction of mass that can develop chaotic diffusion in a Hubble time, i.e. with $L_{\text{cuj}} > 10^{-2}$, as a function of m .

the behavior of the C family but in a lower level (dashed line). From this figure we infer that the mass in chaotic motion at a given time is not a monotonic function of m . There is a value of m (about $m = 0.001$) that favors a larger fraction of mass in chaotic motion with $L_j > 10^{-2.8}$ at $t = 150$.

In Fig. 10b we give the dependence on m of the part of total mass that can develop chaotic diffusion in a Hubble time, i.e. the part that has $L_{\text{cuj}} > 10^{-2}$ in the Q family (solid line) and the C family (dashed line). This part of the total chaotic mass increases abruptly as m increases from 0 to 0.001 and it increases more slowly when m increases further in the Q model, while it remains almost constant in the C model. This behavior

is due to two effects. Namely, as m increases the fraction of mass in chaotic motion (with $L_j > 10^{-2.8}$) at a given snapshot decreases for $m > 0.001$, but on the other hand the maximum of the distribution of the Lyapunov number is transposed to larger values as it is shown in Figs. 11a–d.

In Figs. 11a–d we show the distribution of mass in chaotic motion (normalized to unity) along the values of $\log(L_j)$ in the models Q100, Q050, Q010, Q005 (solid black lines) and the models C100, C050, C010, C005 (dashed red lines), respectively, in their snapshot at $t = 150$. The peak of the distribution is mainly due to the presence of the central mass and appears at larger values of L_j , as m increases. The peaks are almost independent of the type of the model (Q or C).

As regards the distribution of the mass in chaotic motion along the energies, the chaotic orbits cover almost smoothly all the values of binding energies, being more populated in lower energies.

The fractions of mass in chaotic motion and the distribution of the Lyapunov numbers, for the models Q000, Q005, Q010 and C000, C005, C010 vary so slowly that can be considered almost permanent. The secular evolution of such systems is very slow.

The very slow secular evolution of the models with $m < 0.005$ is due to the fact that the majority of the chaotic orbits have Lyapunov numbers (measured either by the L_j s or by the L_{cuj} s) smaller than 10^{-2} (see Figs. 10 and 11). Thus, their diffusion rate in a Hubble time and their possible organization by trapping in SAT type orbits is not important.

This is not the case, however, for larger values of m . As we have seen (Fig. 4) at a time $t = 300$ the model Q100, as well as the models Q050, C050, C100 at a time $t = 2000$, have reached an equilibrium state with a roughly constant value of their triaxiality index T , which is quite different than the value of T at $t = 150$. As these models evolve towards their equilibrium states, their mass components in chaotic motion decrease in time.

We call “equilibrium snapshots” the snapshot at $t = 300$ for Q100 and at $t = 2000$ for Q050, C050, C100 and we find the fraction of mass in chaotic motion in each of these equilibrium snapshots. The detected mass in chaotic motion in Q100 is reduced from $\approx 55\%$ at $t = 150$ to $\approx 22\%$ in the equilibrium snapshot and in Q050 from $\approx 74\%$ to $\approx 25\%$. The respective reduction in C100 is from $\approx 30\%$ to $\approx 12\%$ and in C050 from $\approx 40\%$ to $\approx 19\%$.

Note that, the orbits that remain chaotic in the equilibrium stage are still distributed smoothly all along the axis of binding energies.

It is worth to notice that, for a number of particles the ordered motion may have been changed to chaotic and vice versa, due to the noise of the potential during the self-consistent run. This effect, however, is small. We have checked, for example, that in the Q100 model, 90% of identities of the particles in the fraction 22% (of the mass in chaotic motion in the equilibrium snapshot) coincide with particles that move in chaotic orbits at $t = 150$. Thus, the uncertainty of the fractions of mass in chaotic motion given above is of the order of 1 or 2% of the total mass.

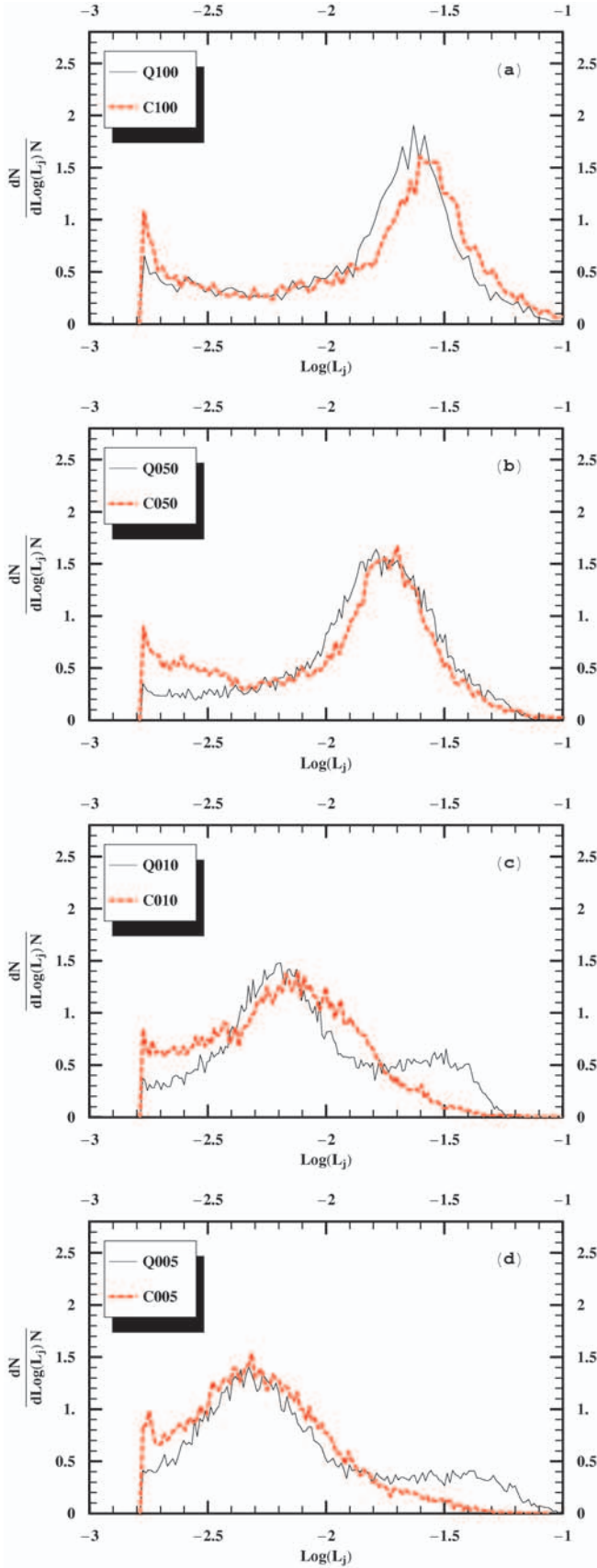


Fig. 11. a)–d) Normalized distributions of the mass in chaotic motion along the L_j axis of the two families of models as indicated in the figures. The maximum of the distribution appears at a value of L_j that depends on m .

The reduction of the mass in chaotic motion in the models Q100, Q050 and C100, C050, can also be seen in the distribution of this mass along the $\log(L_j)$ axis shown in Figs. 12a–d (solid line for the snapshot of $t = 150$ and dashed line for the equilibrium snapshots). The normalization of the distributions to unity is done with respect to the number of chaotic orbits at the snapshot of $t = 150$ for comparison. It is remarkable that the maximum relative reduction is made around the maximum of the distribution. This means that the main part of the mass that has been organized in regular motion comes from the orbits having L_j s in the region of the maximum of their distribution.

6. Self-organization under the presence of a central mass

The fact that the mass component in chaotic motion decreases in time in the above models indicates that these systems are in a process or self-organization in time. This fact reveals the ability of a central mass to organize part of the motion. A number of initially chaotic orbits are converted to ordered orbits. This process occurs at a faster rate for larger m .

In Fig. 13a we give the example of a particle's orbit in the Q000 model, that appears as a typical ordered box orbit. The longest axis of the box is along a direction very close to the z direction. In Fig. 13b we give the orbit of the same particle in the Q100 model. In both cases this orbit is integrated in the self-consistent (time varying) potential of the corresponding system. In the Q000 model the projection of the major axis of the orbit on the yz plane librates relative to the z -axis. When the central mass is inserted (Q100 model) the above libration becomes chaotic with its amplitude increasing on the average. At a given moment, the libration turns to rotation around the x -axis. The line drawn in Fig. 13c shows schematically this change from libration to rotation of the orbit in Fig. 13b. The dots next the numbers 1 to 12 along this line indicate the successive angular positions of every second apocentre of the orbit during the libration period, while the dots next to the numbers 13 to 21 indicate the angular position of the same apocentre as the orbit enters the rotation period. (Notice that while the azimuthal positions of the dots are exact, their radial positions are arbitrary so that the distinction between libration and rotation is more clearly demonstrated.) In its subsequent evolution the orbit becomes ordered, of a SAT type. During the time for which the orbit in Fig. 13b is drawn, the self-consistent potential has changed, so that the equipotential surfaces approach an oblate shape, that increases the area of stability of the SAT orbits.

The above description is better understood in the following way. In Figs. 14a–d we plot the projections of the 4D Poincaré surface of section on the (R, V_R) plane (as in Fig. 6d) derived from the Hamiltonian (14) applied in the Q100 model. The energy level is $H = -74$, equal to the energy of the orbit in Fig. 13b. We use the potential in (14) at four different snapshots of the self-consistent evolution of the Q100 model taken at times $t = 5, 120, 185, 355$ for Figs. 14a–d, respectively.

During the integration of the orbit in Fig. 13b (in the self-consistently varying potential), we collect the Poincaré consequents (R, V_R) of the orbit, every time the orbit crosses the

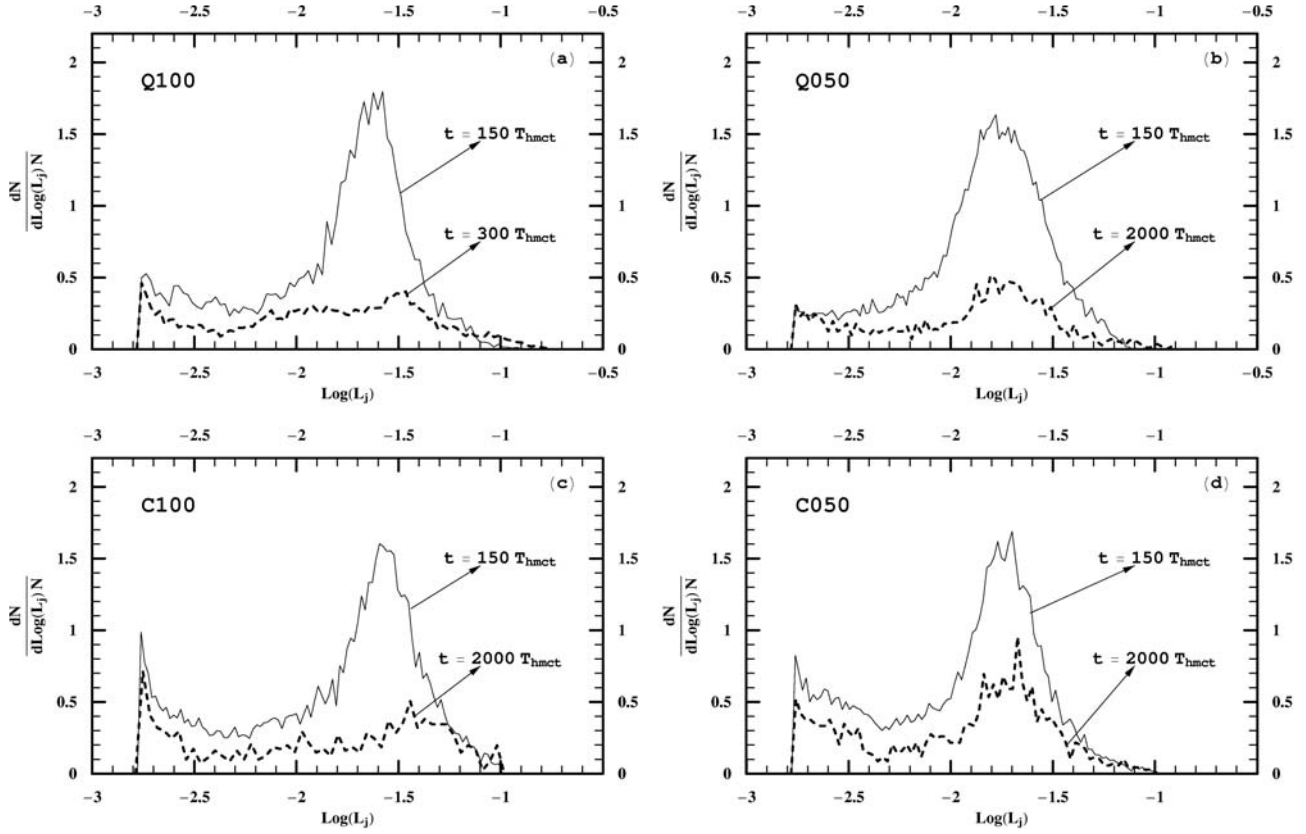


Fig. 12. a)–d) Distribution of the chaotic mass along the L_j axis at the equilibrium stages (dashed lines) in comparison with the corresponding distribution at $t = 150$ (solid lines) normalized to unity, in the case of Q100, Q050, C100, C050 models, respectively. Due to the self-organization, the maximum of the distribution shows a considerable decrease in the equilibrium stage.

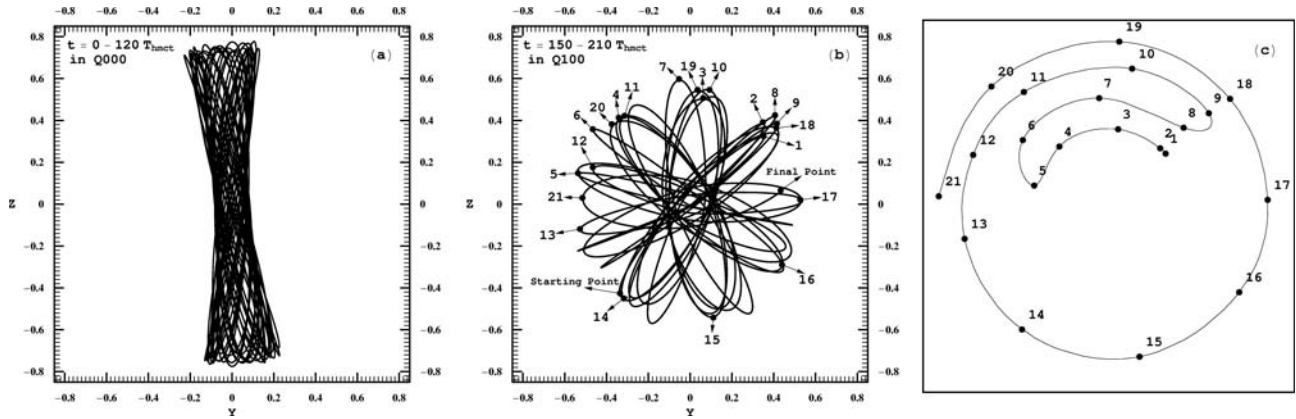


Fig. 13. a) A typical Box orbit of a particle in the self-consistent evolution of the Q000 model. b) The orbit of the same particle run in the self-consistent potential of the Q100 model describes initially a chaotic libration around the z axis with increasing amplitude, converted later on to an ordered rotation around the x axis (SAT type orbit). c) Schematic representation of the angular motion of the major axis of the orbit from a chaotic libration (points with the numbers 1 to 12) to an ordered rotation (points with the numbers 13 to 21).

xy plane, ($z = 0$, with $\dot{z} > 0$). In time $t = 5$ only two consequents were found, plotted in Fig. 14a (red stars). In time $t = 120$ the total number of consequents found was 35, plotted in Fig. 14b by red stars. These consequents fall on the chaotic part of the portrait. Comparing Figs. 14a and 14b, we see that from the snapshot at $t = 5$ to the snapshot at $t = 120$ the size of the island of the SAT orbit has been considerably increased (some of the red stars, that seem to be inside the island, fell there while this region, during this interval of time, was chaotic,

i.e. before the island reached this area). The increase of the island is due to the flattening of the equipotential surfaces that has occurred.

In Fig. 14c (snapshot of the potential at $t = 185$) besides the red stars that correspond to the period of time while the orbit was chaotic, we mark by blue dots the first 4 consequents of the orbit that fall on the well organized area of the island of the SAT orbits. At about this time the libration of the major axis of the orbit in Fig. 13b is converted to rotation.

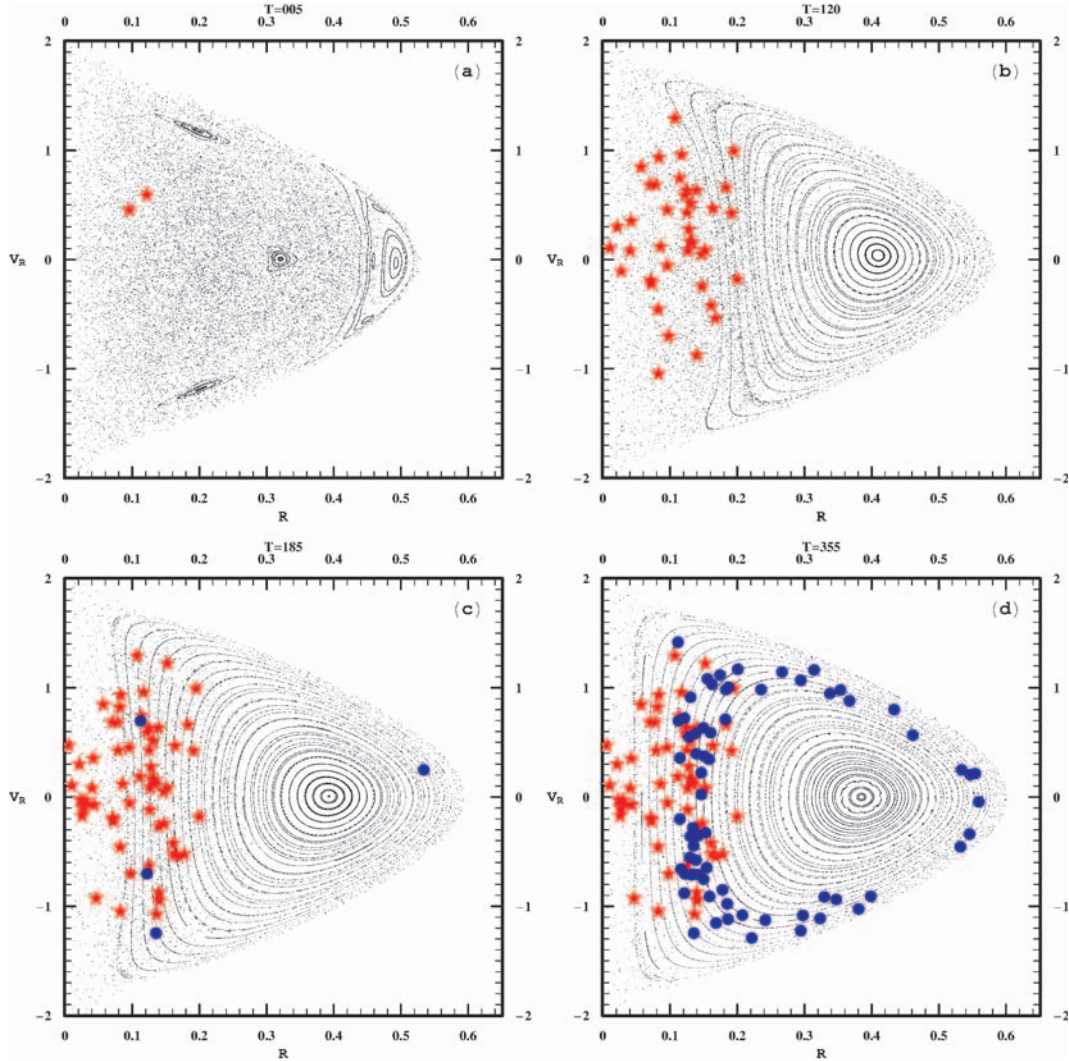


Fig. 14. a)–d) Projections on the (R, V_R) plane of the phase space portrait (as in Fig. 6d) at the snapshots of the self-consistent potential of the Q100 model corresponding to times $t = 5$ in **a)**, $t = 120$ in **b)**, $t = 185$ in **c)** and $t = 355$ in **d)**. The increase of the size of the island of the SAT orbits is due to the change of the shape of the equipotential surfaces. Red stars in these figures give the projections on the same plane of the Poincaré consequents of the chaotic segment of the orbit in Fig. 13b, collected up to the time of the snapshot of the figure. These consequents fall on the chaotic part of the portrait. Some of the red stars, that seem to be inside the island, fell there before the island reached this region. The blue dots give the Poincaré consequents of the ordered segment of the orbit.

In the subsequent evolution of the orbit all the consequents, shown by blue dots in Fig. 14d, fall on the organized area of SAT orbits.

The above example is typical, showing the process of self-organization of the galaxy. A triaxial initial configuration, such as in the Q000 model, under the presence of central mass of relative value $m = 0.01$, becomes unstable. It evolves towards a new equilibrium configuration in which a considerable number of chaotic orbits are converted to SAT orbits.

The presence of a central mass produces entropy in one region of phase space by producing chaos in box or box-like orbits, but at the same time it decreases the entropy in another region of phase space by organizing part of the chaotic motion in SAT orbits.

During this process of self-organization, order is created out of chaos. This is because an internal transfer of energy and entropy occurs from one region of phase space to another.

The energy and entropy transfer occurs via the time variation of the potential. During this self-organization new material, initially moving in chaotic orbits with a box-like geometry, is trapped in SAT type orbits. This causes a variation to the self-consistent potential, by which energy and entropy are transferred from the SAT orbits to the remaining chaotic orbits.

The Lyapunov numbers of many orbits from those that remain chaotic, increase in order to balance the decrease of entropy in the area of SAT orbits. In Figs. 15a,b we show the projection of the particles in the Q100 model on the plane of their binding energy E and their $\log(L_j)$ at the snapshot of time $t = 150$ (Fig. 15a) and the snapshot of $t = 300$ (Fig. 15b). The number of particles that appear to have L_j 's larger than $10^{-2.8}$, i.e. the mass in chaotic motion, is larger in Fig. 15a than in Fig. 15b (as we have seen in Fig. 12a). However, the number of orbits with L_j larger than 10^{-1} is larger in Fig. 15b than in Fig. 15a. In other words, as the mass in chaotic motion

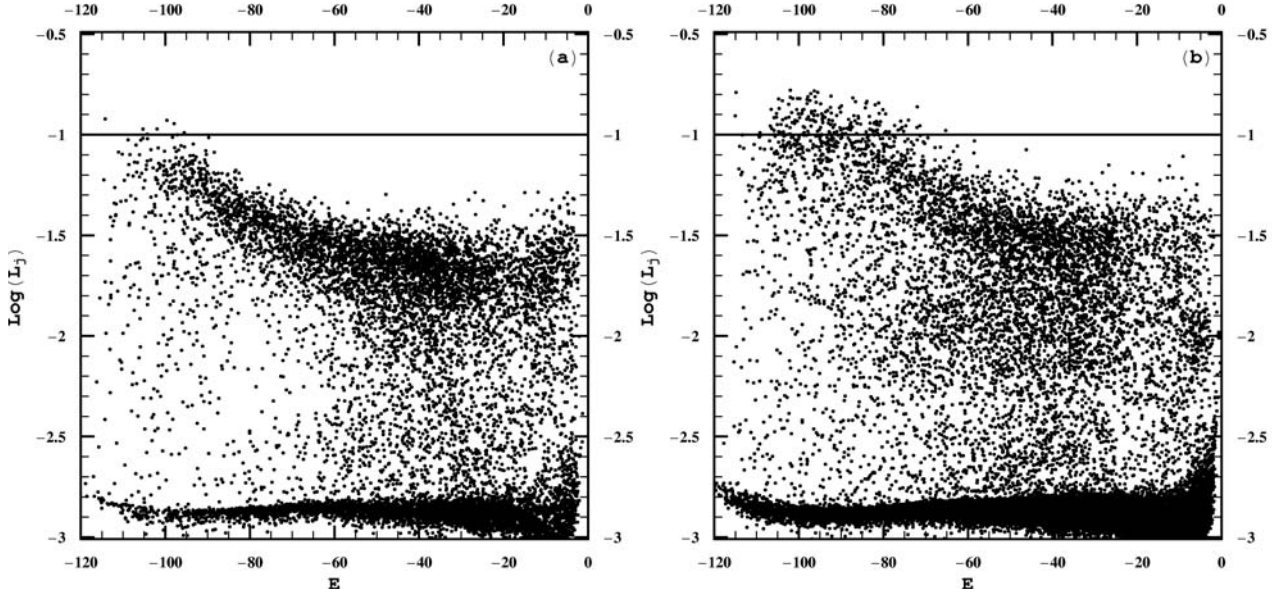


Fig. 15. **a), b)** All the orbits of the system Q100 plotted on the plane $E - \log(L_j)$ of their binding energy E and their $\log(L_j)$, evaluated at $t = 150$ in **a)** and at $t = 300$ in **b)**. The number of chaotic orbits (with $\log(L_j) > -2.8$) is less in **b)** than in **a)** (see Fig. 12a), but, due to the second law of thermodynamics, larger values of L_j appear in **b)** than in **a)**, see, for example, the number of orbits with $\log(L_j) > -1$.

decreases, larger Lyapunov exponents appear in agreement with the second law of Thermodynamics.

Finally, we wish to point out the following remark. A careful examination of the time series of the evolution of the quadrupole coefficients B_{l20} in Fig. 5e for times $t < 300$ shows that these coefficients do not evolve smoothly in time. In Fig. 16 we give in magnification the evolution of the first 10 of these coefficients ($l = 0, 1, \dots, 9$), in the time interval $60 < t < 300$. Each of these coefficients sticks for some (small but not insignificant) time interval at an almost constant value and, rather abruptly, it jumps to a smaller value, where it sticks again and so on, forming in this way stairs with steps of various sizes. Some of such steps are pointed by arrows in Fig. 16. Note that the sticking intervals of the various coefficients appear at the same times. This indicates that the corresponding changes are global occurring simultaneously in all the internal sub-scales of the system. Notice that in the numerical tests (2), (3), (4) presented in Sect. 3.1 such steps still exist.

This remark gives a hint that such a system may evolve by some type of self-organized criticality process. This idea is also supported by the fact that the size of an island of ordered motion (such as the island of the SAT orbits, which is closely connected to the shape of the equipotential surfaces) changes by jumps. A detailed study of this mechanism and its possible relation with the self-organized criticality process will appear elsewhere.

7. Conclusions and discussion

Starting from two types of triaxial non-rotating N -body models of elliptical galaxies with smooth centers, i.e. a model with a large initial ellipticity ($E_{\max} \approx 7$, Q model) and a model with a smaller initial ellipticity ($E_{\max} \approx 3.5$, C model), we have examined their response under the presence of a central mass due

mainly to a central black hole. The relative values m of the central mass we have examined are in the range $[0.0005, 0.01]$. Our main conclusions are summarized as follows:

- i) The presence of a central mass produces initially a large amount of mass in chaotic motion, i.e. of $\approx 80\%$ in the Q model and $\approx 50\%$ in the C model, even in the case of the smallest tested value of m .
- ii) In general, due to this chaotic motion the systems are unstable developing a secular evolution. However, for $m < 0.005$ the fraction of mass able to develop chaotic diffusion in a Hubble time (i.e. $L_{\text{cuj}} > 10^{-2}$) is so small that their secular evolution is too slow to be important in time scales of the order of a Hubble time. Therefore, models with $0.0005 \leq m < 0.005$ are characterized by many chaotic orbits (50%–80%), (with most of them weakly chaotic) and they maintain an almost permanent shape in a Hubble time.
- iii) For $m \geq 0.005$, on the other hand, the secular evolution is faster, leading the system from a prolate or a maximally triaxial shape to an equilibrium configuration which is characterized either by an almost zero triaxiality (oblate) or a modest triaxiality depending on the size of m and the initial maximum ellipticity of the system.
- iv) Provided that the central mass is not very dispersed (as it is the case if it is due mainly to a central black hole), the time needed for this equilibrium to be achieved depends both on m and on the initial maximum ellipticity of the system. For $m = 0.01$, this time is equal to about one Hubble time in the case of large initial ellipticity (as in the Q model), but it is several times larger in the case of smaller initial ellipticity (as in the C model). The different behavior between these two models, although they have quite similar distributions of their Lyapunov numbers at

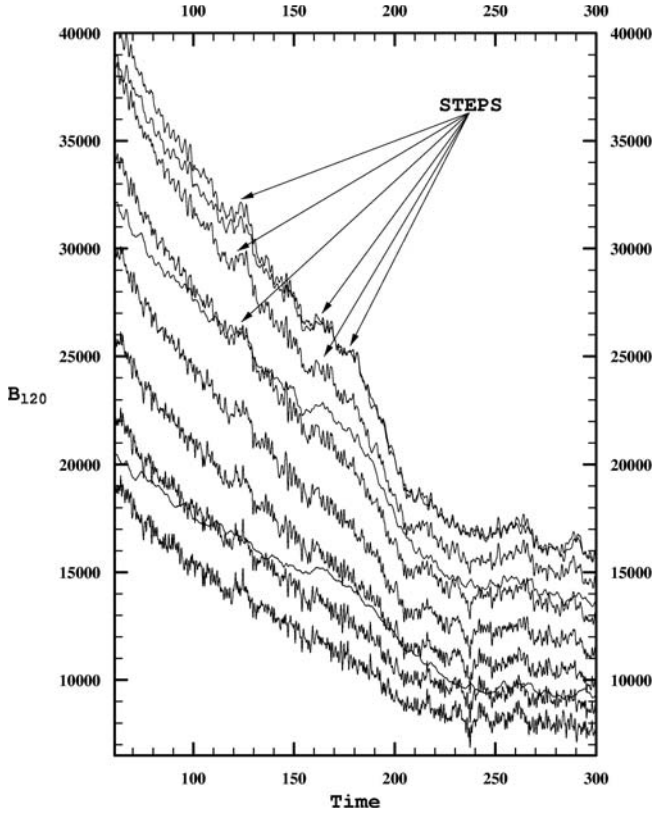


Fig. 16. Magnification of the evolution of the first 10 quadrupole coefficients B_{20} , ($l = 0, 1, \dots, 9$) shown in Fig. 5e in the time interval $60 < t < 300$. Each coefficient sticks for a while at a constant value and, rather abruptly, it jumps to a smaller value, where it sticks again, forming in this way stairs with steps of various sizes. Some of the steps are pointed by arrows in the figure. The sticking intervals appear at the same time for the various coefficients. This is probably a hint that self-organized criticality process takes place.

$t = 150$ (Figs. 11a,b), is due to the fact that they contain different amounts of mass in chaotic motion.

In the case of a more dispersed central mass of the same m the final equilibrium configuration remains almost the same but the time needed for the system to reach this equilibrium is larger. This is due to the smaller values of Lyapunov numbers of the chaotic orbits developed in this case.

v) For $m \geq 0.005$, during the secular evolution of the systems:

a) the fractions of mass in chaotic motion decreases in time and in the equilibrium states it is reduced to the range of 12% to 25%. The systems are self-organized by converting chaotic orbits to ordered orbits of SAT type. This conversion implies transfer of energy and entropy from the region of SAT orbits to the remaining chaotic orbits through the time variation of the self-consistent potential. This implies a local decrease of the entropy that is compatible with the second law of Thermodynamics given that larger values of the Lyapunov numbers appear in the remaining chaotic orbits.

b) the maximum ellipticity decreases in time. The initial ellipticity of the equidensity contours on the plane of shortest-middle axis maintains an almost constant in time value independently of m . This constant value is approached by the maximum ellipticity of the system at the equilibrium configuration.

c) the triaxiality index T decreases. In the case of $m = 0.01$ and large initial maximum ellipticity $E_{\max} \approx 7$ the triaxiality index becomes almost zero within a Hubble time, when the system approaches an oblate spheroidal equilibrium.

The value of $m \approx 0.01$ can be considered as a minimum value of m able to bring an elliptical galaxy to spheroidal equilibrium in a Hubble time. An oblate spheroidal equilibrium can also be obtained for $E_{\max} \approx 3.5$ and $m = 0.01$, or for $E_{\max} \approx 7$ and $m = 0.005$, but this requires times much longer than a Hubble time. In the case of $E_{\max} \approx 3.5$ and $m = 0.005$, the triaxiality index T can be stabilized at larger values (e.g. $T \approx 0.3$), showing that triaxial equilibrium configurations can be compatible with the existence of a massive central mass.

d) the self-organization, at least for the range of parameters in our models, proceeds by jumps indicating that probably a self-organized criticality mechanism takes place.

We have also the following comments:

vi) Our N -Body models are produced from dissipationless collapse and relaxation, therefore they do not make any distinction between the dark and the luminous mass in the galactic models. The values of $m = M_{\text{cm}}/M_g$ are calculated in terms of the total mass M_g of the galaxy inside the radius R_g at which the solution of the Poisson equation joins the solution of the Laplace equation, which is $R_g \approx 6$ in units of the half mass radius.

More convenient for observations is to define an effective relative mass parameter $m_e = M_{\text{cm}}/M_e$, where M_e is the mass inside the bulge of the galaxy or the mass inside a radius defined by the luminous mass. Then our relative mass parameter m can be written as $m = m_e M_e/M_g$ and it may be smaller than the parameter m_e by a factor M_e/M_g depending on the definition of M_e and the mass to light ratio along the radius of the galaxy. If, for example, M_e is defined as the mass inside the half light radius and the mass to light ratio is considered constant along the radius this factor takes the value 0.5. Thus in general m and m_e are of the same order of magnitude, but m_e may be larger by a factor of order 2.

vii) The effect of a large central mass (CM) on the destabilization of the system and the resulting secular evolution depends not only on the size of this mass but also on the types of orbits that already exist in the system. (The sensitivity is larger for larger fractions of mass in box or box-like orbits. These types of orbits are seriously destabilized by the central mass, producing chaotic diffusion and a resulting secular evolution. SAT orbits, on the other hand, as well as OLAT orbits, are further stabilized by the CM,

increasing the stability of the system in their area.) This makes the critical limit of the size of CM, above which secular evolution is considerable in a Hubble time, not very sharp.

- viii) A central mass smaller than this limit cannot produce a dynamical secular evolution, but its presence certainly affects the velocity field of the system in the very central region. The velocity dispersion profile along the projected radius near the center is steeper. One can use this steepening to measure the size of the CM, i.e. of the black hole, as for example, in Magorrian et al. 1998 for real galaxies. Note that the $M_{\text{bh}} - \sigma$ relation found from observational data (e.g. Gebhardt et al. 2000a; Ferrarese & Merritt 2000; Merritt & Ferrarese 2001; Tremaine et al. 2002) shows that the mass of even a small black hole is correlated to the velocity dispersion at radii of the order of the effective radius of the galaxy.
- ix) It is remarkable that the limit of $m \approx 0.005$ found here is of the same order of magnitude as the value found by Magorrian et al. (1998) in real galaxies. This limit may be related to the maximum size to which a central black hole (BH) can grow. Smaller sizes do not convert efficiently the passing-by orbits to SAT orbits, so these orbits can pass many times near the center and increase the probability to be captured by the BH. Such a probability decreases if the BH becomes large enough so that it can change the type of the orbits after only a few near passages.
- x) Finally, if we assume that the galaxy is embedded in a halo a few times more massive than the stellar component (and more extensive) no serious changes are expected in our results. Any possible difference would be due to dark particles moving in high energy orbits, since low energy orbits of dark matter have already been taken into account. Most of the high energy orbits have also large enough angular momenta so that they can hardly approach the center. Their behavior resembles the behavior of the SAT orbits. But even the low angular momentum orbits (of high energy), that can pass near the CM and suffer chaotic deflection, have large radial periods and as a consequence their effective Lyapunov numbers measured by L_{cu} (Sect. 5.1) is too small to produce chaotic diffusion in a Hubble time. Thus an extensive massive dark halo cannot have serious implications as regards the secular evolution of galaxies due to the chaos produced by the CM.

thank the Greek State Scholarship Foundation (I.K.Y) for financial support.

References

- Allen, A. J., Palmer, P. L., & Papaloizou, J. 1990, MNRAS, 242, 576
- Athanassoula, E., Morin, S., Wozniak, H., et al. 1990, MNRAS, 245, 130
- Contopoulos, G., Voglis, N., & Efthymiopoulos, C. 2002, Space Sci. Rev., 102, 37
- Contopoulos, G., Voglis, N., & Kalapotharakos, C. 2002, Celest. Mech. Dyn. Astr., 83, 191
- Cretton, N., & van den Bosch, F. C. 1999, ApJ, 514, 704
- de Zeeuw, T. 1985, MNRAS, 216, 273
- Faber, S. M., Tremaine, S., Ajhar, E. A., et al. 1997, AJ, 114, 1771
- Ferrarese, L., & Merritt, D. 2000, ApJ, 539, 9
- Fridman, T., & Merritt, D. 1997, AJ, 114, 1479
- Gebhardt, K., Bender, R., Bower, G., et al. 2000a, ApJ, 539, 13
- Gebhardt, K., Richstone, D., Kormendy, J., et al. 2000b, AJ, 119, 1157
- Gerhard, O. E., & Binney, J. 1985, MNRAS, 216, 467
- Kandrup, H. E., & Sideris, I. V. 2002, Celest. Mech. Dyn. Astr., 82, 61
- Kandrup, H. E., & Siopis, Ch. 2003, MNRAS, 345, 727
- Kormendy, J., & Richstone, D. 1995, ARA&A, 33, 581
- Kormendy, J., Bender, R., Magorrian, J., et al. 1997, ApJ, 482, 139
- Kormendy, J., Bender, R., Evans, A. S., Richstone, D., et al. 1998, AJ, 115, 1823
- Lynden-Bell, D. 1969, Nature, 223, 690
- Magorrian, J., Tremaine, S., Richstone, D., et al. 1998, AJ, 115, 2285
- Merritt, D., & Ferrarese, L. 2001, ApJ, 547, 140
- Merritt, D., & Fridman, T. 1996, ApJ, 460, 136
- Merritt, D., & Quinlan, G. D. 1998, ApJ, 498, 625
- Merritt, D., & Valluri, M. 1996, ApJ, 471, 82
- Poon, M. Y., & Merritt, D. 2001, ApJ, 549, 192
- Poon, M. Y., & Merritt, D. 2002, ApJ, 568, 89
- Poon, M. Y., & Merritt, D. 2004, ApJ, 606, 774
- Salpeter, E. E. 1964, ApJ, 140, 796
- Schwarzschild, M. 1979, ApJ, 232, 236
- Siopis, Ch. 1999, Ph.D. Thesis, University of Florida
- Siopis, Ch., & Kandrup, H. E. 2000, MNRAS, 319, 43
- Skokos, Ch. 2001, J. Phys. A, 34, 10029
- Statler, T. S. 1987, ApJ, 321, 113
- Tremaine, S., Gebhardt, K., Bender, R., et al. 2002, ApJ, 574, 740
- Valluri, M., & Merritt, D. 1998, ApJ, 506, 686
- van der Marel Roeland, P., de Zeeuw, P. T., & Rix, H. W. 1997, ApJ, 488, 119
- van der Marel Roeland, P., van den Bosch, & Frank, C. 1998, AJ, 116, 2220
- Verdoes Kleijn, G. A., Baum, S. A., de Zeeuw, P. T., & O'Dea, C. P. 1999, AJ, 118, 2592
- Voglis, N., Contopoulos, G., & Efthymiopoulos, C. 1998, Phys. Rev. E, 57, 372
- Voglis, N., Contopoulos, G., & Efthymiopoulos, C. 1999, Celest. Mech. Dyn. Astr., 73, 211
- Voglis, N., Kalapotharakos, C., & Stavropoulos, I. 2002, MNRAS, 337, 619
- Zeldovich, Y. 1964, Sov. Phys. Dokl., 9, 195

Acknowledgements. We wish to thank Drs. A. Allen, P. Palmer and J. Papaloizou for their code. We also wish to thank an anonymous referee for his useful remarks that helped to improve this paper. This work was financially supported partly by the Research Committee of the Academy of Athens (Research Program 200/493). C.K. wishes to